Appl. Math. Mech. -Engl. Ed., **42**(5), 721–746 (2021)

APPLIED MATHEMATICS AND MECHANICS (ENGLISH EDITION)

https://doi.org/10.1007/s10483-021-2733-9

Mathematical modeling and numerical computation of the effective interfacial conditions for Stokes flow on an arbitrarily rough solid surface*

A. T. TRAN[1], H. LE QUANG[2,†], Q. C. HE[2,3], D. H. NGUYEN[1]

1. Research and Application Center for Technology in Civil Engineering, University of Transport and Communications, Hanoi 10000, Vietnam;
2. Laboratoire Modélisation et Simulation Multi-Echelle, Unité Mixte de Recherche 8208, Centre National de la Recherche Scientifique, Université Gustave Eiffel, Marne-la-Vallée F-77454, France;
3. School of Mechanical Engineering, Southwest Jiaotong University, Chengdu 610031, China

(Received Jul. 16, 2020 / Revised Mar. 12, 2021)

Abstract The present work is concerned with a two-dimensional (2D) Stokes flow through a channel bounded by two parallel solid walls. The distance between the walls may be arbitrary, and the surface of one of the walls can be arbitrarily rough. The main objective of this work consists in homogenizing the heterogeneous interface between the rough wall and fluid so as to obtain an equivalent smooth slippery fluid/solid interface characterized by an effective slip length. To solve the corresponding problem, two efficient numerical approaches are elaborated on the basis of the method of fundamental solution (MFS) and the boundary element methods (BEMs). They are applied to different cases where the fluid/solid interface is periodically or randomly rough. The results obtained by the proposed two methods are compared with those given by the finite element method and some relevant ones reported in the literature. This comparison shows that the two proposed methods are particularly efficient and accurate.

Key words effective slip length, method of fundamental solution (MFS), boundary element method (BEM), Stokeslet, micro-channel, fluid/solid interface

Chinese Library Classification O343.3
2010 Mathematics Subject Classification 74Q15

* Citation: TRAN, A. T., LE QUANG, H., HE, Q. C., and NGUYEN, D. H. Mathematical modelling and numerical computation of the effective interfacial conditions for Stokes flow on an arbitrarily rough solid surface. *Applied Mathematics and Mechanics* (*English Edition*), **42**(5), 721–746 (2021) https://doi.org/10.1007/s10483-021-2733-9

† Corresponding author, E-mail: hung.lequang@univ-paris-est.fr

Project supported by the Vietnam National Foundation for Science and Technology Development (NAFOSTED) (No. 107.02-2017.310)

1 Introduction

In mechanics of fluids, the interface between fluid and solid is usually assumed to be smooth. However, in a variety of situations of theoretical or/and practical interest, for example, in the fabrication of superhydrophobic surfaces, this assumption may appear to be no longer valid and the consideration of rough interfaces becomes necessary. More fundamentally, an interface which is nominally smooth at a coarse scale is generally rough at a finer scale. The problem of determining the effective interfacial conditions for an interface at the macroscopic scale while accounting for interfacial roughness at microscopic and mesoscopic scales has been investigated over the past two decades but is still far from being solved. The present work aims to study the problem of a pressure-driven Stokes flow through a channel between two parallel walls in the case where the interface between the fluid and one wall of the channel is arbitrarily rough. This work can be viewed as a continuation of Ref. [1], in which the interfaces were assumed to be periodically rough.

In modeling and simulating the flow of a fluid over a solid surface, the classical uniform fluid/solid interfacial condition is usually adopted in the case where the solid surface is smooth. However, when the solid surface exhibits roughness, the uniform fluid/solid interfacial hypothesis is often no longer applicable and has to be replaced by a mixed or heterogeneous interfacial condition. One efficient way to deal with a rough fluid/solid interface consists in replacing it by a smooth slippery fluid/solid interface characterized by an effective slip length. The problem of determining such an effective slip length for a rough fluid/solid interface has been studied for more than two decades. We cite, for example, Refs. [2]–[8] for the shear-driven Stokes flow and Refs. [9]–[15] for the pressure-driven Stokes flow. In particular, the effective slip lengths of some special microstructures of rough surfaces have been analytically determined by Feuillebois et al.[16] for the case of a Stokes flow through a thin channel between two parallel rough walls. It is useful to remark that, when the channel thickness is thin, there is a mathematical correspondence of the problem of determining the effective slip length to the one of determining the effective bi-dimensional permeability. Consequently, all results obtained for the effective permeability are directly applicable to the effective slip length. In the other "extreme" case where the channel is thick, Belyaev and Vinogradova[13] obtained an analytical expression of the effective slip length for unidirectionally periodic rough surfaces. In addition, by using a semi-analytical method, Vinogradova and Belyaev[15] provided the effective slip length for the case where the channel thickness is arbitrary but the rough surface is only unidirectionally periodic. Recently, in Ref. [1], a semi-analytical method has been proposed to determine the effective slip length for the case where the channel thickness is arbitrary and the rough surface can be periodic along two directions. However, up to now, the works reported in the literature have been limited to the case where the channel thickness is thin or the microstructure of the rough surface is periodic along one direction or two directions. In view of this situation, the present work aims mainly to solve the open problem of pressure-driven and shear-driven Stokes flows through a channel of arbitrary thickness between two parallel walls whose surfaces are arbitrarily rough. To achieve this objective, we develop, in particular, two approaches to homogenizing a rough interface so as to replace it by an equivalent smooth interface characterized by an effective slip length.

The first approach to be elaborated is based on the method of fundamental solution (MFS). The latter, which can be considered as one of the boundary-discretization methods (without needing to discretize the computational domain), has emerged as an efficient technique for numerically calculating a fluid flow in recent years. We can cite here, for example, the investigations[17–21]. In these studies, the MFS was applied to solve two-dimensional (2D) or three-dimensional (3D) Stokes flows. The specific feature of the MFS resides in using a set of singularized force elements of unknown intensities located at the source points to induce the flow fields. When these intensities are determined, the fluid quantities, such as velocity,

pressure, and stress, can be approximated by employing the free-space Green's functions, called also Stokeslets. In the approach based on the MFS, the collocation points and source points have the same number and are placed on the physical boundary and the fictitious boundary, respectively (see Fig. 1(a)); the force strength can be determined with the aid of the boundary conditions for the whole of collocation points.

In this study, we develop an extended MFS, called XMFS, based on the classical MFS, and use it to compute the velocity and pressure solution fields of a Stokes flow through a parallel-plate channel of arbitrary channel thickness. In the XMFS, instead of Stokeslet, Green's function for a semi-infinite space is used, which includes the effect of one wall in the solution. The modified Green's function has the advantage that the number of discrete points is reduced, yielding a less number of unknown strength.

In the second approach to be proposed, we use the boundary element method (BEM) to solve the boundary integral equation (BIE) governing a Stokes flow in a confined 2D domain. This method has been successfully used for laminar incompressible flows in many previous investigations[22–26]. The BEM is one of the most efficient numerical techniques for solving a BIE. In this equation, the solution fields are presented in terms of integrals (integral representations of the solution), involving the unknown tractions and velocities over the boundaries (also called boundary values). These boundary values are then obtained by solving a system of linear equations, which results from matching the prescribed boundary conditions. Finally, the fluid quantities in the domain are computed by the associated integral representation of the solution. It is well-known that singular integrals are a difficulty needed to overcome when using the BEM, and the accuracy in evaluating them is essential to obtaining accurate solutions. In this work, these singular integrals are evaluated analytically. An important distinction between the MFS and the BEM is that the boundary in the MFS is discretized discontinuously by a system of collocation points and no mesh is required, while the boundary in the BEM is divided successively into a finite number of segments, which are called boundary elements (see Fig. 1(b)).

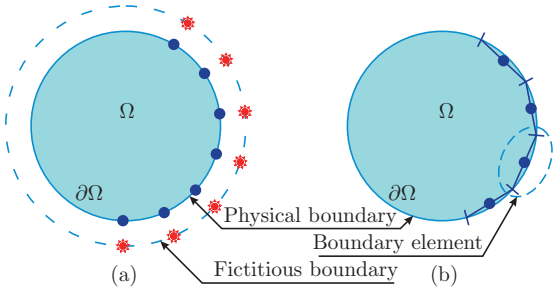

Fig. 1 Discretization schematic of (a) MFS and (b) BEM (color online)

The paper is organized as follows. In Section 2, the setting of the problem under investigation is specified. In particular, the local governing equations, the description of the rough interface, and the macroscopic constitutive equations are given. Section 3 is dedicated to elaborating the approaches based on the MFS and XMFS to determine the velocity solution field of the Stokes flow and to find the effective slip length for the rough interface. Section 4 describes the details of the BEM and the relevant procedure for computing the effective slip length. In Section 5, the derived results for the effective slip length of a rough interface obtained from the two elaborated approaches are compared with the corresponding numerical results obtained by the finite element method and the main relevant results reported in the literature. Finally, a few concluding remarks are provided in Section 6.

2 Problem setting

In this work, we consider a 2D steady Stokes flow through a channel between two parallel walls of distance $\widehat{H}$ and length $\widehat{W}$. The fluid, with its dynamic viscosity denoted by μ and confined in the channel, is assumed to be incompressible, Newtonian, and driven either by an applied pressure gradient of intensity ρ or by a translation with a constant speed $\widehat{U}^* = \rho\widehat{W}\widehat{H}/\mu$ of the upper channel's wall.

At the microscopic scale, the interface between the Stokes flow and the top wall of this channel is assumed to be smooth, and a no-slip interfacial condition is adopted to characterize this interface. In contrast with the top wall, the bottom interface between the Stokes flow and the bottom wall of the channel is considered to be rough, and a mixed interfacial condition is now applied at this bottom interface. Precisely, the bottom interface is assumed to be decomposed of n interfacial regions, each of which is characterized by its intrinsic (or microscopic) slip length, denoted by $\widehat{\lambda}_s$ $(s = 1, 2, \cdots, n)$.

Next, we denote by Ω the 2D domain occupied by a representative surface element (RSE) of the Stokes flow confined in the channel. We designate by $\partial\Omega^{\mathrm{T}}$ and $\partial\Omega^{\mathrm{B}}$ the top and bottom interfaces between the Stokes flow and the top and bottom walls of the channel, respectively. Let $\{\widehat{x}\widehat{y}\}$ be a 2D cartesian coordinate system associated with Ω in such a way that the $\widehat{x}$-direction represents the flow direction and the top wall is located at $\widehat{y} = \widehat{\omega}$ whereas the bottom wall is situated at $\widehat{y} = \widehat{\omega} - \widehat{H}$ (see Fig. 2).

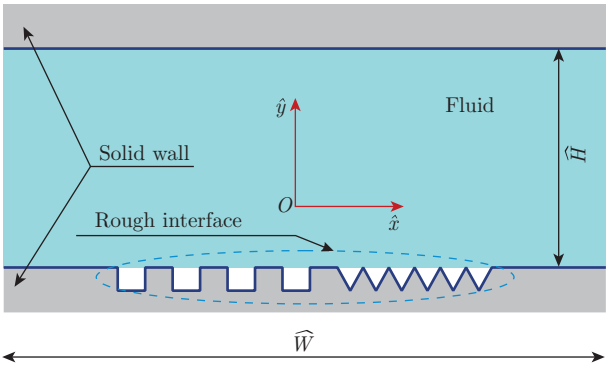

Fig. 2 Problem schematic: Stokes flow inside a channel with non-homogeneous boundary conditions (color online)

The Stokes equations governing the fluid flow under consideration take the following form:

$$\mu\Delta\widehat{\boldsymbol{U}}(\widehat{\boldsymbol{x}}) = \nabla\widehat{p}(\widehat{\boldsymbol{x}}), \tag{1}$$

$$\nabla\cdot\widehat{\boldsymbol{U}}(\widehat{\boldsymbol{x}}) = 0, \tag{2}$$

where $\widehat{\boldsymbol{U}}(\widehat{\boldsymbol{x}}) = \big(\widehat{U}(\widehat{\boldsymbol{x}}), \widehat{V}(\widehat{\boldsymbol{x}})\big)$ denotes the velocity vector field, and $\widehat{p}(\widehat{\boldsymbol{x}})$ designates the pressure field of the 2D fluid flow.

In addition, the velocity vector of the Stokes flow must verify the following boundary conditions at the top and bottom interfaces:

(i) At the top smooth interface $\partial\Omega^{\mathrm{T}}$, the no-penetration and no-slip conditions imply that

$$\widehat{\boldsymbol{U}}(\widehat{\boldsymbol{x}}) = \boldsymbol{0}. \tag{3}$$

(ii) At the bottom rough interface $\partial\Omega^{\mathrm{B}} = \bigcup_{s=1}^{n} \partial\Omega_s^{\mathrm{B}}$, the no-penetration and slip conditions can be expressed by

$$\widehat{\boldsymbol{U}}(\widehat{\boldsymbol{x}})\cdot\boldsymbol{n}(\widehat{\boldsymbol{x}}) = 0, \tag{4}$$

$$\widehat{\boldsymbol{U}}(\widehat{\boldsymbol{x}})\cdot\boldsymbol{t}(\widehat{\boldsymbol{x}})=\widehat{\lambda}(\widehat{\boldsymbol{x}})\big(-\widehat{\boldsymbol{\sigma}}(\widehat{\boldsymbol{x}})\cdot\boldsymbol{n}(\widehat{\boldsymbol{x}})\big)\cdot\boldsymbol{t}(\widehat{\boldsymbol{x}}),\tag{5}$$

where $\boldsymbol{n}(\widehat{\boldsymbol{x}})$ is the unit vector normal to the boundary, oriented from the fluid into the bottom wall, $\boldsymbol{t}(\widehat{\boldsymbol{x}})$ is the unit tangential vector in the anti-clockwise direction, and the local slip length $\widehat{\lambda}(\widehat{\boldsymbol{x}})$ of the bottom interface is characterized by $\widehat{\lambda}(\widehat{\boldsymbol{x}})=\widehat{\lambda}_s$ if $\widehat{\boldsymbol{x}}\in\partial\Omega_s^{\mathrm{B}}$. $\widehat{\boldsymbol{\sigma}}$ denotes the stress tensor field in the fluid.

At the macroscopic scale, the bottom rough interface between the fluid and the inferior wall of the channel is homogenized so as to be replaced with an equivalent smooth interface whose effective interfacial condition is expressed by

$$\big\langle\widehat{\boldsymbol{U}}(\widehat{\boldsymbol{x}})\cdot\boldsymbol{t}(\widehat{\boldsymbol{x}})\big\rangle=\widehat{b}\big(-\widehat{\boldsymbol{\sigma}}(\widehat{\boldsymbol{x}})\cdot\boldsymbol{n}(\widehat{\boldsymbol{x}})\big)\cdot\boldsymbol{t}(\widehat{\boldsymbol{x}})\big\rangle\quad\text{with}\quad\widehat{\boldsymbol{x}}=(\widehat{x},\widehat{\omega}-\widehat{H}),\tag{6}$$

where $\widehat{b}$ is defined as the effective slip length of the equivalent smooth interface, and the symbol $\langle*\rangle$ denoting the length average of a local quantity $*$ on the bottom interface characterized by $\widehat{y}=\widehat{\omega}-\widehat{H}$ is defined by

$$\langle*\rangle=\frac{1}{|\partial\Omega^{\mathrm{B}}|}\int_{\partial\Omega^{\mathrm{B}}}*\,\mathrm{d}\widehat{\boldsymbol{x}},\tag{7}$$

where $|\partial\Omega^{\mathrm{B}}|$ designates the length of $\partial\Omega^{\mathrm{B}}$.

Due to the fact that the Stokes flow problem is linear, the superposition principle can be applied by decomposing the velocity vector field $\widehat{\boldsymbol{U}}(\widehat{\boldsymbol{x}})$ into two parts as follows:

$$\widehat{\boldsymbol{U}}(\widehat{\boldsymbol{x}})=\widehat{\boldsymbol{u}}^{\mathrm{H}}(\widehat{\boldsymbol{x}})+\widehat{\boldsymbol{u}}(\widehat{\boldsymbol{x}}).\tag{8}$$

Here, $\widehat{\boldsymbol{u}}^{\mathrm{H}}(\widehat{\boldsymbol{x}})$ is the homogeneous part of the velocity field obtained when no-slip interfacial conditions are applied at both the top and bottom interfaces. It is clear that $\widehat{\boldsymbol{u}}^{\mathrm{H}}(\widehat{\boldsymbol{x}})$ corresponds exactly to the classical solution of the Poiseuille or Couette flow. The second part $\widehat{\boldsymbol{u}}(\widehat{\boldsymbol{x}})$, viewed as the perturbation part of the velocity vector solution and due to the presence of the roughness on the bottom fluid/solid interface, will be determined exhaustively in the next two sections. It is well-known that, under an applied pressure gradient or a translation of upper wall, the velocity vector field, $\widehat{\boldsymbol{u}}^{\mathrm{P}}(\widehat{\boldsymbol{x}})$ and $\widehat{\boldsymbol{u}}^{\mathrm{C}}(\widehat{\boldsymbol{x}})$, of the classical Poiseuille and Couette flow are given by

$$\widehat{\boldsymbol{u}}^{\mathrm{H}}(\widehat{\boldsymbol{x}})=\begin{cases}\widehat{\boldsymbol{u}}^{\mathrm{P}}(\widehat{\boldsymbol{x}})=(\widehat{u}^{\mathrm{P}},0)\quad\text{for the Poiseuille flow,}\\ \widehat{\boldsymbol{u}}^{\mathrm{C}}(\widehat{\boldsymbol{x}})=(\widehat{u}^{\mathrm{C}},0)\quad\text{for the Couette flow}\end{cases}\tag{9}$$

with

$$\widehat{u}^{\mathrm{P}}=-\frac{\rho(\widehat{y}+\widehat{H}-\widehat{\omega})^2}{2\mu}+\frac{\rho\widehat{H}(\widehat{y}+\widehat{H}-\widehat{\omega})}{2\mu},\tag{10}$$

$$\widehat{u}^{\mathrm{C}}(\widehat{\boldsymbol{x}})=\frac{\rho\widehat{W}(\widehat{y}+\widehat{H}-\widehat{\omega})}{\mu}.\tag{11}$$

3 MFS

3.1 Classical MFS

The perturbation part $\widehat{\boldsymbol{u}}(\widehat{\boldsymbol{x}})$ of the velocity vector $\widehat{\boldsymbol{U}}(\widehat{\boldsymbol{x}})$ and the pressure field $\widehat{p}(\widehat{\boldsymbol{x}})$ can be determined by applying the MFS. For the bi-dimensional case, according to this method, the source point $\widehat{\boldsymbol{\xi}}_j=(\widehat{\xi}_j,\widehat{\eta}_j)$ $(j=1,2,\cdots,N)$ with unknown strength $\widehat{\boldsymbol{\tau}}_j=(\widehat{\tau}_j,\widehat{\nu}_j)$ is located outside the flow domain and situated at an artificial boundary of distance $\widehat{\varepsilon}$ between the fictitious and physical boundaries. For simplicity, the source points are assumed to be regularly distributed at this fictitious boundary. By applying the superposition principle, the perturbation

part of the velocity vector solution field can be determined at any point of observation $\widehat{\boldsymbol{x}} \in \Omega$ by the following approximation:

$$\widehat{\boldsymbol{u}}(\widehat{\boldsymbol{x}}) = \frac{1}{4\pi\mu}\sum_{j=1}^{N} \widehat{\boldsymbol{S}}(\widehat{\boldsymbol{x}}, \widehat{\boldsymbol{\xi}}_j)\widehat{\boldsymbol{\tau}}_j(\widehat{\boldsymbol{\xi}}_j), \tag{12}$$

where $\widehat{\boldsymbol{S}}(\widehat{\boldsymbol{x}}, \widehat{\boldsymbol{\xi}})$ is the individual free-space Green's tensor function associated with the velocity vector field, called also Stokeslet (see Ref. [27]). Physically, the component $\widehat{S}_{\alpha\beta}(\widehat{\boldsymbol{x}}, \widehat{\boldsymbol{\xi}})$ of $\widehat{\boldsymbol{S}}(\widehat{\boldsymbol{x}}, \widehat{\boldsymbol{\xi}})$ with α and β given by x or y represents the value of the velocity vector at the observation point $\widehat{\boldsymbol{x}}$ in the α-direction due to a point source of unit strength applied at $\widehat{\boldsymbol{\xi}}$ in the β-direction. More precisely, the expressions of $\widehat{\boldsymbol{S}}(\widehat{\boldsymbol{x}}, \widehat{\boldsymbol{\xi}})$ take the following form:

$$\widehat{S}_{\alpha\beta}(\widehat{\boldsymbol{x}}, \widehat{\boldsymbol{\xi}}) = -\delta_{\alpha\beta}\ln\widehat{r} + \frac{\widehat{r}_\alpha \widehat{r}_\beta}{\widehat{r}^2}. \tag{13}$$

In this equation, $\widehat{\boldsymbol{r}} = \widehat{\boldsymbol{x}} - \widehat{\boldsymbol{\xi}}$, $\widehat{r} = \|\widehat{\boldsymbol{r}}\|$, and $\delta_{\alpha\beta}$ stands for Kronecker's symbol if $\delta_{xx} = \delta_{yy} = 1$ and $\delta_{\alpha\beta} = 0$ otherwise. By choosing $\widehat{W}$ as the length scale and ρ as the reference of pressure gradient, we obtain the following dimensionless parameters:

$$\begin{cases} x = \widehat{x}/\widehat{W}, \quad y = \widehat{y}/\widehat{W}, \quad H = \widehat{H}/\widehat{W}, \quad \xi = \widehat{\xi}/\widehat{W}, \quad \eta = \widehat{\eta}/\widehat{W}, \\ u = \widehat{u}\mu/(\rho\widehat{W}^2), \quad v = \widehat{v}\mu/(\rho\widehat{W}^2), \quad \tau = \widehat{\tau}/(\rho\widehat{W}^2), \quad \nu = \widehat{\nu}/(\rho\widehat{W}^2). \end{cases}$$

Therefore, the perturbation part of the velocity vector field takes the following dimensionless form:

$$u(x,y) = \frac{1}{4\pi}\sum_{j=1}^{N}\Big(\Big(\frac{(x-\xi_j)^2}{r_j^2} - \ln r_j\Big)\tau_j + \Big(\frac{(x-\xi_j)(y-\eta_j)}{r_j^2}\Big)\nu_j\Big), \tag{14}$$

$$v(x,y) = \frac{1}{4\pi}\sum_{j=1}^{N}\Big(\Big(\frac{(x-\xi_j)(y-\eta_j)}{r_j^2}\Big)\tau_j + \Big(\frac{(y-\eta_j)^2}{r_j^2} - \ln r_j\Big)\nu_j\Big). \tag{15}$$

To determine the unknown strength $\boldsymbol{\tau}_j$ with $j = 1, 2, \cdots, N$, the same number of boundary collocation points $\boldsymbol{x}_i$ $(i = 1, 2, \cdots, N)$ distributed on the physical boundary $\partial\Omega$ should be considered (see Fig. 3). Note that N is the total number of collocation points determined by

$$N = N^{\mathrm{T}} + N^{\mathrm{B}} \quad \text{with} \quad N^{\mathrm{B}} = \sum_{s=1}^{n} N_s, \tag{16}$$

where N^{T} and N^{B} are the numbers of collocation points on the two top and bottom interfaces, $\partial\Omega^{\mathrm{T}}$ and $\partial\Omega^{\mathrm{B}}$, respectively, and N_s corresponds to the number of collocation points on the sth interfacial region $\partial\Omega_s^{\mathrm{B}}$ of the bottom wall. Then, the boundary conditions (3)–(5) of the perturbation flow at the top and bottom interfaces can be expressed in the equivalent dimensionless forms as follows:

(i) At the top smooth interface $\partial\Omega^{\mathrm{T}}$,

$$u(x_k, \omega) = v(x_k, \omega) = 0. \tag{17}$$

(ii) At the bottom rough interface $\partial\Omega^{\mathrm{B}} = \bigcup_{s=1}^{n} \partial\Omega_s^{\mathrm{B}}$,

$$v(x_i, \omega - H) = 0, \tag{18}$$

$$u(x_i, \omega - H) = \lambda_i\Big(\frac{\partial u}{\partial y}(x_i, \omega - H) + \chi\Big), \tag{19}$$

where $\chi = H/2$ for the pressure-driven flow, $\chi = 1$ for the shear-driven flow, and $\lambda_i = \widehat{\lambda}_i/\widehat{W}$ is the normalized intrinsic slip length at an arbitrary point $\boldsymbol{x}_i = (x_i, \omega - H) \in \partial\Omega_s^{\mathrm{B}}$. By applying the point collocation method[5], a set containing N^{T} collocation points $\boldsymbol{x}_i$ $(i = 1, 2, \cdots, N^{\mathrm{T}})$ situated at the top interface $\partial\Omega^{\mathrm{T}}$ and a set comprising N^{B} collocation points $\boldsymbol{x}_i$ $(i = 1, 2, \cdots, N^{\mathrm{B}})$ located at the bottom interface of the channel are introduced. For simplicity, the collocation points are assumed to be regularly distributed at the top and bottom interfaces $\partial\Omega^{\mathrm{T}}$ and $\partial\Omega^{\mathrm{B}}$. Accounting for the boundary conditions (17)–(19), we obtain the following system of equations with $2N$ unknown strengths $\{\tau_j, \nu_j\}$ for the 2D Stokes flow problem:

(i) At the top smooth interface $\partial\Omega^{\mathrm{T}}$,

$$\sum_{j=1}^{N}\Big(\frac{(x_i-\xi_j)^2}{r_{ij}^2} - \ln r_{ij}\Big)\tau_j + \sum_{j=1}^{N}\Big(\frac{(x_i-\xi_j)(y_i-\eta_j)}{r_{ij}^2}\Big)\nu_j = 0, \tag{20}$$

$$\sum_{j=1}^{N}\Big(\frac{(x_i-\xi_j)(y_i-\eta_j)}{r_{ij}^2}\Big)\tau_j + \sum_{j=1}^{N}\Big(\frac{(y_i-\eta_j)^2}{r_{ij}^2} - \ln r_{ij}\Big)\nu_j = 0. \tag{21}$$

(ii) At the bottom rough interface $\partial\Omega^{\mathrm{B}}$,

$$\begin{aligned}&\sum_{j=1}^{N}\Big(\frac{(x_i-\xi_j)^2}{r_{ij}^2} - \ln r_{ij} + \lambda_i\frac{(y_i-\eta_j)}{r_{ij}^2} + \lambda_i\frac{2(x_i-\xi_j)^2(y_i-\eta_j)}{r_{ij}^4}\Big)\tau_j\\ &+\sum_{j=1}^{N}\Big(\frac{(x_i-\xi_j)(y_i-\eta_j)}{r_{ij}^2} - \lambda_i\frac{(x_i-\xi_j)}{r_{ij}^2} + \lambda_i\frac{2(x_i-\xi_j)(y_i-\eta_j)^2}{r_{ij}^4}\Big)\nu_j = 4\pi\lambda_i\chi,\end{aligned} \tag{22}$$

$$\sum_{j=1}^{N}\Big(\frac{(x_i-\xi_j)(y_i-\eta_j)}{r_{ij}^2}\Big)\tau_j + \sum_{j=1}^{N}\Big(\frac{(y_i-\eta_j)^2}{r_{ij}^2} - \ln r_{ij}\Big)\nu_j = 0, \tag{23}$$

where r_{ij} is the distance from the source point j to the observation point i.

The system of $2N$ linear equations (20)–(23) can be recast in the matrix form as follows:

$$\boldsymbol{A}\boldsymbol{\tau} = \boldsymbol{c}, \tag{24}$$

where $\boldsymbol{A}$ is a $2N \times 2N$ matrix, $\boldsymbol{c}$ is a vector of $2N$ components whose expressions take the right-hand side of Eqs. (20)–(23), and $\boldsymbol{\tau} = \{\tau_1, \tau_2, \cdots, \tau_N, \nu_1, \nu_2, \cdots, \nu_N\}^{\mathrm{T}}$ represents the unknown strength vector. The expressions of $\boldsymbol{A}$ and $\boldsymbol{c}$ can be found in Appendix A.

Finally, the solution provided by the system of linear equations (24) allows us to calculate the velocity solution field through Eq. (8) together with Eqs. (10), (11), (14), and (15). The effective normalized slip length can be determined by using the following equivalent form of Eq. (6):

$$b = \frac{\displaystyle\sum_{i=1}^{N^{\mathrm{B}}} u(x_i, \omega - H)}{\displaystyle\sum_{i=1}^{N^{\mathrm{B}}}\Big(\frac{\partial u}{\partial y}(x_i, \omega - H) + \chi\Big)}. \tag{25}$$

3.2 XMFS

It should be mentioned here that the classical MFS previously established requires a discretization of collocation points at both the top and bottom interfaces between the flow and two walls of the channel. However, in this paper, because the top interface between the flow and the bottom wall of the channel is assumed to be smooth and non-slippery, we are interested only to determine the effective interfacial condition of the bottom rough interface. Hence, instead

of the free-space Green's function employed in the previous section, we propose now to use the new Green's function associated with a domain bounded by a solid plane wall (see Refs. [22] and [27]). This Green's function allows us to reduce the quantity as well as the times of calculation by incorporating the effect of the top wall into the fundamental solution. Therefore, only the bottom interface must be discretized. This discretization is illustrated in Fig. 4.

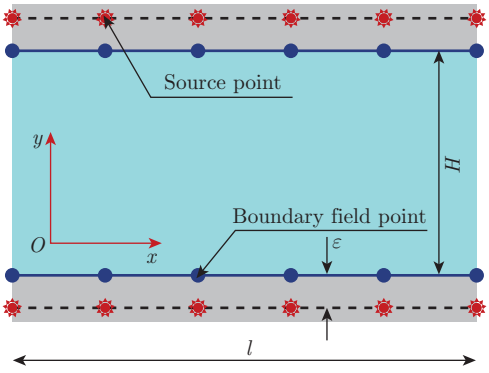

Fig. 3 Distribution of boundary field points and source points (color online)

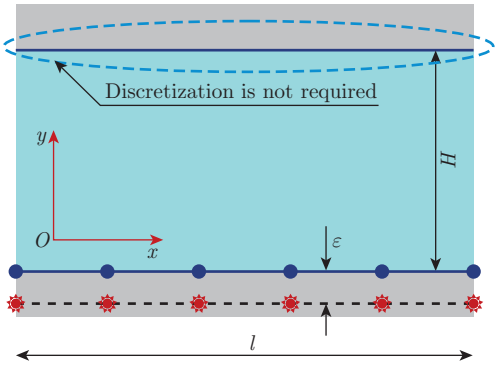

Fig. 4 Discretization of the bottom rough interface and distribution of source points (color online)

Here, let us assume that the perturbation part of the velocity solution field is induced by an array of source points $\widehat{\boldsymbol{\xi}}_j$ $(j = 1, 2, \cdots, N^{\mathrm{B}})$ located at the distance $\varepsilon = \widehat{\varepsilon}/\widehat{W}$ from the bottom wall (see Fig. 4). Therefore, the perturbation part of the velocity field can be expressed as

$$\widehat{\boldsymbol{u}}(\widehat{\boldsymbol{x}}) = \frac{1}{4\pi\mu}\sum_{j=1}^{N^{\mathrm{B}}} \widehat{\boldsymbol{G}}^{W}(\widehat{\boldsymbol{x}}, \widehat{\boldsymbol{\xi}}_j)\widehat{\boldsymbol{\tau}}(\widehat{\boldsymbol{\xi}}_j). \tag{26}$$

In this equation, the individual Green's function $\widehat{\boldsymbol{G}}^{W}(\widehat{\boldsymbol{x}}, \widehat{\boldsymbol{\xi}}_j)$ represents the velocity field at $\widehat{\boldsymbol{x}}$ of the fluid bounded by a plane wall located at $\widehat{y} = \widehat{\omega}$ produced by a unit force at a source point $\widehat{\boldsymbol{\xi}}_j$. This individual Green's function can be expressed as the sum of four contributions as

$$\widehat{\boldsymbol{G}}^{W}(\widehat{\boldsymbol{x}}, \widehat{\boldsymbol{\xi}}) = \widehat{\boldsymbol{S}}(\widehat{\boldsymbol{x}}, \widehat{\boldsymbol{\xi}}) - \widehat{\boldsymbol{S}}(\widehat{\boldsymbol{x}}, \widehat{\boldsymbol{\xi}}') + 2\widehat{h}^2\widehat{\boldsymbol{G}}^{\mathrm{D}}(\widehat{\boldsymbol{x}}, \widehat{\boldsymbol{\xi}}') - 2\widehat{h}\widehat{\boldsymbol{G}}^{\mathrm{SD}}(\widehat{\boldsymbol{x}}, \widehat{\boldsymbol{\xi}}'), \tag{27}$$

where $\widehat{\boldsymbol{\xi}}'$ is the mirror image of the source point $\widehat{\boldsymbol{\xi}}$ with respect to the upper wall (see Fig. 5), $\widehat{h} = \widehat{\eta} - \widehat{\omega}$, and the tensors $\widehat{\boldsymbol{G}}^{\mathrm{D}}(\widehat{\boldsymbol{x}}, \widehat{\boldsymbol{\xi}})$ and $\widehat{\boldsymbol{G}}^{\mathrm{SD}}(\widehat{\boldsymbol{x}}, \widehat{\boldsymbol{\xi}}')$ are defined as

$$\widehat{G}^{\mathrm{D}}_{\alpha\beta}(\widehat{\boldsymbol{x}}, \widehat{\boldsymbol{\xi}}') = \kappa\frac{\partial}{\partial\widehat{R}_\beta}\Big(\frac{\widehat{R}_\alpha}{\widehat{R}^2}\Big) = \kappa\Big(\frac{\delta_{\alpha\beta}}{\widehat{R}^2} - 2\frac{\widehat{R}_\alpha\widehat{R}_\beta}{\widehat{R}^4}\Big), \tag{28}$$

$$\widehat{G}^{\mathrm{SD}}_{\alpha\beta}(\widehat{\boldsymbol{x}}, \widehat{\boldsymbol{\xi}}') = \kappa\frac{\partial}{\partial\widehat{R}_\beta}\widehat{S}_{\alpha y}(\widehat{\boldsymbol{x}}, \widehat{\boldsymbol{\xi}}') = \widehat{R}_y\widehat{G}^{\mathrm{D}}_{\alpha\beta}(\widehat{\boldsymbol{x}}, \widehat{\boldsymbol{\xi}}') + \kappa\frac{\delta_{\beta y}\widehat{R}_\alpha - \delta_{\alpha y}\widehat{R}_\beta}{\widehat{R}^2}. \tag{29}$$

In Eqs. (28) and (29),

$$\begin{cases} \kappa = \begin{cases} 1, & \beta = x, \\ -1, & \beta = y, \end{cases} \\ \widehat{\boldsymbol{R}} = \widehat{\boldsymbol{x}} - \widehat{\boldsymbol{\xi}}', \quad \widehat{R}_x = \widehat{x} - \widehat{\xi}, \quad \widehat{R}_y = \widehat{y} + \widehat{\eta} - 2\widehat{\omega}, \quad \widehat{R} = \|\widehat{\boldsymbol{R}}\|. \end{cases}$$

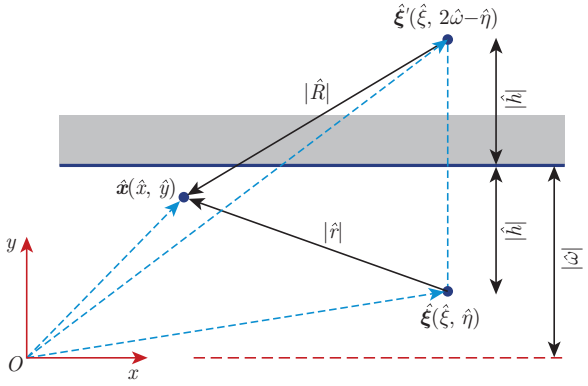

Fig. 5 Location of Stokeslet and image for a computation of Green's function in a semi-infinite space (color online)

The formulae of the perturbation part of the velocity vector field are now expressed in the dimensionless forms by using the same normalized parameters proposed in the previous subsection,

$$u(x,y)=\frac{1}{4\pi}\sum_{j=1}^{N^{\mathrm{B}}}((G^W_{xx}(\boldsymbol{x},\boldsymbol{\xi}_j)\tau_j+G^W_{xy}(\boldsymbol{x},\boldsymbol{\xi}_j)\nu_j), \tag{30}$$

$$v(x,y)=\frac{1}{4\pi}\sum_{j=1}^{N^{\mathrm{B}}}(G^W_{yx}(\boldsymbol{x},\boldsymbol{\xi}_j)\tau_j+G^W_{yy}(\boldsymbol{x},\boldsymbol{\xi}_j)\nu_j), \tag{31}$$

where the expressions of $G^W_{\alpha\beta}(\boldsymbol{x},\boldsymbol{\xi}_j)$ are detailed by

$$\begin{aligned}G^W_{xx}(\boldsymbol{x},\boldsymbol{\xi}_j)\ =\ &\frac{(x-\xi_j)^2}{r_j^2}-\ln r_j-\frac{(x-\xi_j)^2}{R_j^2}+\ln R_j+2h_j^2\Big(\frac{1}{R_j^2}-\frac{2(x-\xi_j)^2}{R_j^4}\Big)\\&-2h_j\Big(\frac{(y+\eta_j-2\omega)}{R_j^2}-\frac{2(x-\xi_j)^2(y+\eta_j-2\omega)}{R_j^4}\Big),\end{aligned} \tag{32}$$

$$\begin{aligned}G^W_{xy}(\boldsymbol{x},\boldsymbol{\xi}_j)\ =\ &\frac{(x-\xi_j)(y-\eta_j)}{r_j^2}-\frac{(x-\xi_j)(y+\eta_j-2\omega)}{R_j^2}+4h_j^2\frac{(x-\xi_j)(y+\eta_j-2\omega)}{R_j^4}\\&+2h_j\Big(\frac{(x-\xi_j)}{R_j^2}-\frac{2(x-\xi_j)(y+\eta_j-2\omega)^2}{R_j^4}\Big),\end{aligned} \tag{33}$$

$$\begin{aligned}G^W_{yx}(\boldsymbol{x},\boldsymbol{\xi}_j)\ =\ &\frac{(x-\xi_j)(y-\eta_j)}{r_j^2}-\frac{(x-\xi_j)(y+\eta_j-2\omega)}{R_j^2}-4h_j^2\frac{(x-\xi_j)(y+\eta_j-2\omega)}{R_j^4}\\&+2h_j\Big(\frac{(x-\xi_j)}{R_j^2}+\frac{2(x-\xi_j)(y+\eta_j-2\omega)^2}{R_j^4}\Big),\end{aligned} \tag{34}$$

$$\begin{aligned}G^W_{yy}(\boldsymbol{x},\boldsymbol{\xi}_j)\ =\ &\frac{(y-\eta_j)^2}{r_j^2}-\ln r_j-\frac{(y+\eta_j-2\omega)^2}{R_j^2}+\ln R_j-2h_j^2\Big(\frac{1}{R_j^2}-\frac{2(y+\eta_j-2\omega)^2}{R_j^4}\Big)\\&+2h_j\Big(\frac{(y+\eta_j-2\omega)}{R_j^2}-\frac{2(y+\eta_j-2\omega)^3}{R_j^4}\Big)\end{aligned} \tag{35}$$

with $h_j = \eta_j - \omega$.

Next, the $2N^{\mathrm{B}}$ unknown strengths $\{\tau_j, \nu_j\}$ with $j = 1, 2, \cdots, N^{\mathrm{B}}$ related to N^{B} source point $\boldsymbol{\xi}_j$ are determined by applying once more the point collocation method presented in the previous section. However, in the present case, the collocation points are distributed only at the bottom boundary $\partial\Omega^{\mathrm{B}}$ and the number of the collocation points $\boldsymbol{x}_i$ $(i = 1, 2, \cdots, N^{\mathrm{B}})$ is chosen in such a way that it is equal to the number of the source points. The interfacial conditions (18) and (19) at $\partial\Omega^{\mathrm{B}}$ must be satisfied at all interfacial points. This yields a system of $2N^{\mathrm{B}}$ linear equations as follows:

$$\sum_{j=1}^{N^{\mathrm{B}}} \Big(G^W_{xx}(\boldsymbol{x}_i, \boldsymbol{\xi}_j) - \lambda_i \frac{\partial G^W_{xx}}{\partial y}(\boldsymbol{x}_i, \boldsymbol{\xi}_j) \Big) \tau_j$$

$$+ \sum_{j=1}^{N^{\mathrm{B}}} \Big(G^W_{xy}(\boldsymbol{x}_i, \boldsymbol{\xi}_j) - \lambda_i \frac{\partial G^W_{xy}}{\partial y}(\boldsymbol{x}_i, \boldsymbol{\xi}_j) \Big) \nu_j = 4\pi\lambda_i\chi, \tag{36}$$

$$\sum_{j=1}^{N^{\mathrm{B}}} G^W_{yx}(\boldsymbol{x}_i, \boldsymbol{\xi}_j)\tau_j + \sum_{j=1}^{N^{\mathrm{B}}} G^W_{yy}(\boldsymbol{x}, \boldsymbol{\xi}_j)\nu_j = 0. \tag{37}$$

This system can be rewritten in the equivalent matrix form as

$$\boldsymbol{A}'\boldsymbol{\tau} = \boldsymbol{c}', \tag{38}$$

where $\boldsymbol{A}'$ and $\boldsymbol{c}'$ are a $2N^{\mathrm{B}} \times 2N^{\mathrm{B}}$ matrix and a column vector of $2N^{\mathrm{B}}$ components, respectively, and $\boldsymbol{\tau}$ is a column vector of unknown strengths $\{\tau_k, \nu_k\}$ with $k = 1, 2, \cdots, N^{\mathrm{B}}$. The expressions of the components of $\boldsymbol{A}'$ and $\boldsymbol{c}'$ are provided in Appendix B.

Similar to Subsection 3.1, after solving the system of linear equations (38), the same procedure can be applied to calculate the velocity solution field and the effective normalized slip length b.

It is important to notice that the advantage of using Green's function for a semi-infinite flow consists in reducing the number of source points considered and, thus, in reducing the number of unknown strengths. This is achieved by incorporating the no-slip interfacial condition on the top wall into the formulation. Therefore, the size of matrix $\boldsymbol{A}'$ is less than that of $\boldsymbol{A}$ with the same number of discretization points on the bottom interface $\partial\Omega^{\mathrm{B}}$. This diminishes the time and memory needed for calculations.

4 BEM

In this section, the perturbation part of the velocity solution field will be calculated by using an approach based on the BEM, sometimes called also the boundary integral method. There are many studies demonstrating the efficiency and accuracy of this method in finding the solution to the Stokes flow in 2D channels[22–24,28]. In these studies, Green's function for a domain between two infinite plane walls was used, and there was no need for a discretization of these walls. Inspired by the aforementioned works, we propose in this section to use Green's function for a semi-infinite fluid domain bounded by a plane wall.

The perturbation part $\widehat{\boldsymbol{u}}(\widehat{\boldsymbol{x}}_0)$ of the velocity solution field at an arbitrary point $\widehat{\boldsymbol{x}}_0$ in a domain of fluid bounded by an infinite plan wall can be transformed into a boundary integral representation of solution as follows[27]:

$$\epsilon(\widehat{\boldsymbol{x}}_0)\widehat{\boldsymbol{u}}(\widehat{\boldsymbol{x}}_0) = -\frac{1}{4\pi\mu}\int_{\partial\Omega^{\mathrm{B}}} \widehat{\boldsymbol{\tau}}(\widehat{\boldsymbol{x}}) \cdot \widehat{\boldsymbol{\mathcal{G}}}(\widehat{\boldsymbol{x}}, \widehat{\boldsymbol{x}}_0)\mathrm{d}l(\widehat{\boldsymbol{x}}) - \frac{1}{4\pi}\int_{\partial\Omega^{\mathrm{B}}} \widehat{\boldsymbol{u}}(\widehat{\boldsymbol{x}}) \cdot \big(\widehat{\boldsymbol{\mathcal{T}}}(\widehat{\boldsymbol{x}}, \widehat{\boldsymbol{x}}_0) \cdot \boldsymbol{n}(\widehat{\boldsymbol{x}})\big)\mathrm{d}l(\widehat{\boldsymbol{x}}), \tag{39}$$

where $\epsilon(\widehat{\boldsymbol{x}}_0)$ is a parameter depending on the position of the source point $\widehat{\boldsymbol{x}}_0$ given by

$$\epsilon(\widehat{\boldsymbol{x}}_0)=\begin{cases}1 & \text{for } \widehat{\boldsymbol{x}}_0 \text{ inside } \Omega,\\ \dfrac{1}{2} & \text{for } \widehat{\boldsymbol{x}}_0 \text{ on the smooth boundary } \partial\Omega^{\mathrm{B}},\end{cases} \tag{40}$$

and $\widehat{\boldsymbol{\mathcal{G}}}(\widehat{\boldsymbol{x}},\widehat{\boldsymbol{x}}_0)$ is either the velocity Green's function for a semi-infinite domain of the fluid bounded by a plane wall $\widehat{\boldsymbol{G}}^{W}(\widehat{\boldsymbol{x}},\widehat{\boldsymbol{x}}_0)$ defined by Eq. (27) or the periodic velocity Green's function for the flow in a semi-infinite domain $\widehat{\boldsymbol{G}}^{W\mathrm{P}}(\widehat{\boldsymbol{x}},\widehat{\boldsymbol{x}}_0)$ given by

$$\widehat{\boldsymbol{G}}^{W\mathrm{P}}(\widehat{\boldsymbol{x}},\widehat{\boldsymbol{x}}_0)=\widehat{\boldsymbol{S}}^{\mathrm{P}}(\widehat{\boldsymbol{x}},\widehat{\boldsymbol{x}}_0)-\widehat{\boldsymbol{S}}^{\mathrm{P}}(\widehat{\boldsymbol{x}},\widehat{\boldsymbol{x}}_0')+2\widehat{h}^2\widehat{\boldsymbol{G}}^{\mathrm{DP}}(\widehat{\boldsymbol{x}},\widehat{\boldsymbol{x}}_0')-2\widehat{h}\widehat{\boldsymbol{G}}^{\mathrm{SDP}}(\widehat{\boldsymbol{x}},\widehat{\boldsymbol{x}}_0'), \tag{41}$$

where $\widehat{\boldsymbol{S}}^{\mathrm{P}}(\widehat{\boldsymbol{x}},\widehat{\boldsymbol{x}}_0')$ stands for the periodic Green's function in the free space,

$$\widehat{\boldsymbol{S}}^{\mathrm{P}}(\widehat{\boldsymbol{x}},\widehat{\boldsymbol{x}}_0')=\widehat{\boldsymbol{S}}^{\mathrm{P}}(\widehat{\boldsymbol{x}}-\widehat{\boldsymbol{x}}_0')=\widehat{\boldsymbol{S}}^{\mathrm{P}}(\boldsymbol{X})=\begin{bmatrix}-\mathcal{A}-Y\mathcal{A}_Y+1 & Y\mathcal{A}_X\\ Y\mathcal{A}_X & -\mathcal{A}+Y\mathcal{A}_Y\end{bmatrix}, \tag{42}$$

where

$$\mathcal{A}(\boldsymbol{X})=\frac{1}{2}\ln\left(\cosh\left(kY\right)-\cos\left(kX\right)\right)+\frac{1}{2}\ln 2,\quad \mathcal{A}_X=\frac{\partial\mathcal{A}}{\partial X},\quad \mathcal{A}_Y=\frac{\partial\mathcal{A}}{\partial Y} \tag{43}$$

with $k=2\pi$ denoting the wave number. In addition, the normalized period of the flow is equal to one. The tensors $\widehat{\boldsymbol{G}}^{\mathrm{DP}}(\widehat{\boldsymbol{x}},\widehat{\boldsymbol{x}}_0')$ and $\widehat{\boldsymbol{G}}^{\mathrm{SDP}}(\widehat{\boldsymbol{x}},\widehat{\boldsymbol{x}}_0')$ are determined by

$$\widehat{\boldsymbol{G}}^{\mathrm{DP}}(\widehat{\boldsymbol{x}},\widehat{\boldsymbol{x}}_0')=\widehat{\boldsymbol{G}}^{\mathrm{DP}}(\boldsymbol{X})=\begin{bmatrix}-\mathcal{A}_{YY} & -\mathcal{A}_{XY}\\ \mathcal{A}_{XY} & -\mathcal{A}_{YY}\end{bmatrix}, \tag{44}$$

$$\widehat{\boldsymbol{G}}^{\mathrm{SDP}}(\widehat{\boldsymbol{x}},\widehat{\boldsymbol{x}}_0')=\widehat{\boldsymbol{G}}^{\mathrm{SDP}}(\boldsymbol{X})=\begin{bmatrix}-Y\mathcal{A}_{YY} & -\mathcal{A}_X-Y\mathcal{A}_{XY}\\ -\mathcal{A}_X+Y\mathcal{A}_{XY} & -Y\mathcal{A}_{YY}\end{bmatrix} \tag{45}$$

with

$$\begin{cases}\mathcal{A}_{XY}=\dfrac{\partial^2\mathcal{A}}{\partial X\partial Y},\\ \mathcal{A}_{YY}=\dfrac{\partial^2\mathcal{A}}{\partial Y^2}.\end{cases}$$

The stress tensor $\widehat{\boldsymbol{\mathcal{T}}}(\widehat{\boldsymbol{x}},\widehat{\boldsymbol{x}}_0)$ in Eq. (39) can be expressed into the two following cases: (i) when an arbitrary flow is considered, the stress tensor corresponds exactly to the stress Green's function $\widehat{\boldsymbol{T}}^{W}(\widehat{\boldsymbol{x}},\widehat{\boldsymbol{x}}_0)$ for a semi-infinite domain bounded by a solid wall, i.e., $\widehat{\boldsymbol{\mathcal{T}}}(\widehat{\boldsymbol{x}},\widehat{\boldsymbol{x}}_0)=\widehat{\boldsymbol{T}}^{W}(\widehat{\boldsymbol{x}},\widehat{\boldsymbol{x}}_0)$; (ii) when a periodic flow is concerned, the stress tensor becomes the periodic stress Green's function $\widehat{\boldsymbol{T}}^{W\mathrm{P}}(\widehat{\boldsymbol{x}},\widehat{\boldsymbol{x}}_0)$, i.e., $\widehat{\boldsymbol{\mathcal{T}}}(\widehat{\boldsymbol{x}},\widehat{\boldsymbol{x}}_0)=\widehat{\boldsymbol{T}}^{W\mathrm{P}}(\widehat{\boldsymbol{x}},\widehat{\boldsymbol{x}}_0)$. These two functions $\widehat{\boldsymbol{T}}^{W}(\widehat{\boldsymbol{x}},\widehat{\boldsymbol{x}}_0)$ and $\widehat{\boldsymbol{T}}^{W\mathrm{P}}(\widehat{\boldsymbol{x}},\widehat{\boldsymbol{x}}_0)$ are given as follows:

(i) When an arbitrary flow is considered,

$$\widehat{\boldsymbol{T}}^{W}(\widehat{\boldsymbol{x}},\widehat{\boldsymbol{x}}_0)=\widehat{\boldsymbol{T}}(\widehat{\boldsymbol{x}},\widehat{\boldsymbol{x}}_0)-\widehat{\boldsymbol{T}}(\widehat{\boldsymbol{x}},\widehat{\boldsymbol{x}}_0')+2\widehat{h}^2\widehat{\boldsymbol{T}}^{\mathrm{D}}(\widehat{\boldsymbol{x}},\widehat{\boldsymbol{x}}_0')-2\widehat{h}\widehat{\boldsymbol{T}}^{\mathrm{SD}}(\widehat{\boldsymbol{x}},\widehat{\boldsymbol{x}}_0'), \tag{46}$$

where the components of $\widehat{\boldsymbol{T}}(\widehat{\boldsymbol{x}},\widehat{\boldsymbol{x}}_0)$, called the free-space stresslet, are defined by

$$\widehat{T}_{\alpha\beta\gamma}(\widehat{\boldsymbol{x}},\widehat{\boldsymbol{x}}_0)=-4\frac{\widehat{r}_\alpha\widehat{r}_\beta\widehat{r}_\gamma}{\widehat{r}^4}, \tag{47}$$

while $\widehat{\boldsymbol{T}}^{\mathrm{D}}(\widehat{\boldsymbol{x}},\widehat{\boldsymbol{x}}_0')$ and $\widehat{\boldsymbol{T}}^{\mathrm{SD}}(\widehat{\boldsymbol{x}},\widehat{\boldsymbol{x}}_0')$ are two tensors whose components are determined by

$$\begin{cases} \widehat{T}^{\mathrm{D}}_{\alpha\beta\gamma}(\widehat{\boldsymbol{x}},\widehat{\boldsymbol{x}}_0) = \dfrac{\partial \widehat{G}^{\mathrm{D}}_{\alpha\beta}}{\partial \widehat{R}_\gamma} + \dfrac{\partial \widehat{G}^{\mathrm{D}}_{\gamma\beta}}{\partial \widehat{R}_\alpha}, \\ \widehat{T}^{\mathrm{SD}}_{\alpha\beta\gamma}(\widehat{\boldsymbol{x}},\widehat{\boldsymbol{x}}_0) = -\delta_{\alpha\gamma}\widehat{p}^{\mathrm{SD}}_\beta + \dfrac{\partial \widehat{G}^{\mathrm{SD}}_{\alpha\beta}}{\partial \widehat{R}_\gamma} + \dfrac{\partial \widehat{G}^{\mathrm{SD}}_{\gamma\beta}}{\partial \widehat{R}_\alpha}. \end{cases} \tag{48}$$

In Eq. (48), $\widehat{p}^{\mathrm{SD}}_\beta$ is the pressure field corresponding to the Stokeslet doublet, given by

$$\widehat{p}^{\mathrm{SD}}_\alpha(\widehat{\boldsymbol{x}},\widehat{\boldsymbol{x}}_0') = 2\kappa \frac{\partial}{\partial \widehat{R}_\alpha}\Big(\frac{\widehat{R}_y}{\widehat{R}^2}\Big) = 2\kappa\Big(\frac{\delta_{\alpha y}}{\widehat{R}^2} - 2\frac{\widehat{R}_\alpha \widehat{R}_y}{\widehat{R}^4}\Big), \tag{49}$$

and

$$\begin{cases} \widehat{\boldsymbol{r}} = \widehat{\boldsymbol{x}} - \widehat{\boldsymbol{x}}_0, \quad \widehat{r} = |\widehat{\boldsymbol{r}}|, \quad \widehat{r}_x = \widehat{x} - \widehat{x}_0, \quad \widehat{r}_y = \widehat{y} - \widehat{y}_0, \\ \widehat{\boldsymbol{R}} = \widehat{\boldsymbol{x}} - \widehat{\boldsymbol{x}}_0', \quad \widehat{R} = |\widehat{\boldsymbol{R}}|, \quad \widehat{R}_x = \widehat{r}_x, \quad \widehat{R}_y = \widehat{y} + \widehat{y}_0 - 2\widehat{\omega}. \end{cases}$$

(ii) When a periodic flow is concerned,

$$\widehat{\boldsymbol{T}}^{WP}(\widehat{\boldsymbol{x}},\widehat{\boldsymbol{x}}_0) = \widehat{\boldsymbol{T}}^{\mathrm{P}}(\widehat{\boldsymbol{x}},\widehat{\boldsymbol{x}}_0) - \widehat{\boldsymbol{T}}^{\mathrm{P}}(\widehat{\boldsymbol{x}},\widehat{\boldsymbol{x}}_0') + 2\widehat{h}^2\widehat{\boldsymbol{T}}^{\mathrm{DP}}(\widehat{\boldsymbol{x}},\widehat{\boldsymbol{x}}_0') - 2\widehat{h}\widehat{\boldsymbol{T}}^{\mathrm{SDP}}(\widehat{\boldsymbol{x}},\widehat{\boldsymbol{x}}_0'), \tag{50}$$

where $\widehat{\boldsymbol{T}}^{\mathrm{P}}(\widehat{\boldsymbol{x}},\widehat{\boldsymbol{x}}_0)$, $\widehat{\boldsymbol{T}}^{\mathrm{DP}}(\widehat{\boldsymbol{x}},\widehat{\boldsymbol{x}}_0')$, and $\widehat{\boldsymbol{T}}^{\mathrm{SDP}}(\widehat{\boldsymbol{x}},\widehat{\boldsymbol{x}}_0')$ are, respectively, the periodic Stresslet, the potential dipole periodic of stress, and the Stresslet doublet periodic, whose components are specified by

$$\begin{cases} \widehat{T}^{\mathrm{P}}_{xxx} = -4\mathcal{A}_X - 2Y\mathcal{A}_{XY}, \quad \widehat{T}^{\mathrm{P}}_{xxy} = -2\mathcal{A}_Y + 2Y\mathcal{A}_{XX}, \\ \widehat{T}^{\mathrm{P}}_{yyy} = -2\mathcal{A}_Y - 2Y\mathcal{A}_{XX}, \quad \widehat{T}^{\mathrm{P}}_{xyy} = \widehat{T}^{\mathrm{P}}_{yxy} = 2Y\mathcal{A}_{XY}, \\ \widehat{T}^{\mathrm{P}}_{yyx} = 2Y\mathcal{A}_{XY}, \quad \widehat{T}^{\mathrm{P}}_{xyx} = \widehat{T}^{\mathrm{P}}_{yxx} = -2\mathcal{A}_Y + 2Y\mathcal{A}_{XX}, \end{cases} \tag{51}$$

$$\begin{cases} \widehat{T}^{\mathrm{DP}}_{xxx} = -2\mathcal{A}_{XYY}, \quad \widehat{T}^{\mathrm{DP}}_{xxy} = \mathcal{A}_{XYX} - \mathcal{A}_{YYY}, \\ \widehat{T}^{\mathrm{DP}}_{xyx} = -2\mathcal{A}_{XYX}, \quad \widehat{T}^{\mathrm{DP}}_{xyy} = -2\mathcal{A}_{XYY}, \quad \widehat{T}^{\mathrm{DP}}_{yxx} = \mathcal{A}_{XYX} - \mathcal{A}_{YYY}, \\ \widehat{T}^{\mathrm{DP}}_{yxy} = 2\mathcal{A}_{XYY}, \quad \widehat{T}^{\mathrm{DP}}_{yyx} = -2\mathcal{A}_{XYY}, \quad \widehat{T}^{\mathrm{DP}}_{yyy} = -2\mathcal{A}_{YYY}, \end{cases} \tag{52}$$

$$\begin{cases} \widehat{T}^{\mathrm{SDP}}_{xxx} = -2\mathcal{A}_{XY} - 2Y\mathcal{A}_{XYY}, \\ \widehat{T}^{\mathrm{SDP}}_{xxy} = -\mathcal{A}_{XX} - \mathcal{A}_{YY} + Y\mathcal{A}_{XYX} - Y\mathcal{A}_{YYY}, \\ \widehat{T}^{\mathrm{SDP}}_{xyx} = -2\mathcal{A}_{XX} + 2\mathcal{A}_{YY} - 2Y\mathcal{A}_{XYX}, \\ \widehat{T}^{\mathrm{SDP}}_{yxx} = -\mathcal{A}_{XX} - \mathcal{A}_{YY} + Y\mathcal{A}_{XYX} - Y\mathcal{A}_{YYY}, \\ \widehat{T}^{\mathrm{SDP}}_{xyy} = -2\mathcal{A}_{XY} - 2Y\mathcal{A}_{XYY}, \quad \widehat{T}^{\mathrm{SDP}}_{yxy} = -2\mathcal{A}_{XY} + 2Y\mathcal{A}_{XYY}, \\ \widehat{T}^{\mathrm{SDP}}_{yyx} = -2\mathcal{A}_{XY} - 2Y\mathcal{A}_{XYY}, \quad \widehat{T}^{\mathrm{SDP}}_{yyy} = -2Y\mathcal{A}_{YYY}, \end{cases} \tag{53}$$

where

$$\mathcal{A}_{XX} = \frac{\partial^2 \mathcal{A}}{\partial X^2}, \quad \mathcal{A}_{XYY} = \frac{\partial^3 \mathcal{A}}{\partial X \partial Y^2}, \quad \mathcal{A}_{XYX} = \frac{\partial^3 \mathcal{A}}{\partial X^2 \partial Y}, \quad \mathcal{A}_{YYY} = \frac{\partial^3 \mathcal{A}}{\partial Y^3}.$$

Similar to the aforementioned section, the length, the velocity, the traction, the velocity Green's function, and the stress Green's function can be normalized into dimensionless forms by $\widehat{W}$, $\rho\widehat{W}^2/\mu$, $\rho\widehat{W}$, μ, and $1/\widehat{W}$ in the equations obtained above, respectively. Next, the BIE (39) will be solved numerically by applying the BEM for the dimensionless boundary values $\{\boldsymbol{\tau}(\boldsymbol{x}), \boldsymbol{u}(\boldsymbol{x})\}$. Here, the bottom wall $\partial\Omega^{\mathrm{B}}$ of the channel is decomposed into N^{B} boundary elements Γ_j. The velocity vector of each element can be determined from the ones of its node's values by adopting a constant, linear, or parabolic function. In our investigation, for simplicity, the geometry of the boundary segment can be considered as a straight line (characterized by end points and the node point, see Fig. 6), while the boundary value is assumed to be constant along this straight line and is exactly equal to its node's value. By placing $\boldsymbol{x}_0$ successively at all nodal points $\boldsymbol{x}_{0i}$ $(i = 1, 2, \cdots, N^{\mathrm{B}})$ on the boundary $\partial\Omega^{\mathrm{B}}$, the $2 \times N^{\mathrm{B}}$ BIEs including $4 \times N^{\mathrm{B}}$ unknowns $\{\tau_j, \nu_j, u_j, v_j\}$ are obtained as follows:

$$\begin{aligned}\frac{1}{2}u_i = &-\frac{1}{4\pi}\sum_{j=1}^{N^{\mathrm{B}}}\tau_j\int_{\Gamma_j}G_{xx}(\boldsymbol{x}_j,\boldsymbol{x}_{0i})\mathrm{d}l_j-\frac{1}{4\pi}\sum_{j=1}^{N^{\mathrm{B}}}\nu_j\int_{\Gamma_j}G_{yx}(\boldsymbol{x}_j,\boldsymbol{x}_{0i})\mathrm{d}l_j\\ &-\frac{1}{4\pi}\sum_{j=1}^{N^{\mathrm{B}}}u_j\int_{\Gamma_j}(T_{xxx}(\boldsymbol{x}_j,\boldsymbol{x}_{0i})n_x(\boldsymbol{x}_j)+T_{xxy}(\boldsymbol{x}_j,\boldsymbol{x}_{0i})n_y(\boldsymbol{x}_j))\mathrm{d}l_j\\ &-\frac{1}{4\pi}\sum_{j=1}^{N^{\mathrm{B}}}v_j\int_{\Gamma_j}(T_{yxx}(\boldsymbol{x}_j,\boldsymbol{x}_{0i})n_x(\boldsymbol{x}_j)+T_{yxy}(\boldsymbol{x}_j,\boldsymbol{x}_{0i})n_y(\boldsymbol{x}_j))\mathrm{d}l_j,\end{aligned}\tag{54}$$

$$\begin{aligned}\frac{1}{2}v_i = &-\frac{1}{4\pi}\sum_{j=1}^{N^{\mathrm{B}}}\tau_j\int_{\Gamma_j}G_{xy}(\boldsymbol{x}_j,\boldsymbol{x}_{0i})\mathrm{d}l_j-\frac{1}{4\pi}\sum_{j=1}^{N^{\mathrm{B}}}\nu_j\int_{\Gamma_j}G_{yy}(\boldsymbol{x}_j,\boldsymbol{x}_{0i})\mathrm{d}l_j\\ &-\frac{1}{4\pi}\sum_{j=1}^{N^{\mathrm{B}}}u_j\int_{\Gamma_j}(T_{xyx}(\boldsymbol{x}_j,\boldsymbol{x}_{0i})n_x(\boldsymbol{x}_j)+T_{xyy}(\boldsymbol{x}_j,\boldsymbol{x}_{0i})n_y(\boldsymbol{x}_j))\mathrm{d}l_j\\ &-\frac{1}{4\pi}\sum_{j=1}^{N^{\mathrm{B}}}v_j\int_{\Gamma_j}(T_{yyx}(\boldsymbol{x}_j,\boldsymbol{x}_{0i})n_x(\boldsymbol{x}_j)+T_{yyy}(\boldsymbol{x}_j,\boldsymbol{x}_{0i})n_y(\boldsymbol{x}_j))\mathrm{d}l_j,\end{aligned}\tag{55}$$

where τ_j, ν_j, u_j, and v_j are the nodal values of the jth element for the traction and the velocities along the x- and y-directions, and $\boldsymbol{x}_{0i}$ is the nodal coordinates of the ith element, while the point $\boldsymbol{x}_j$ varies over the jth element.

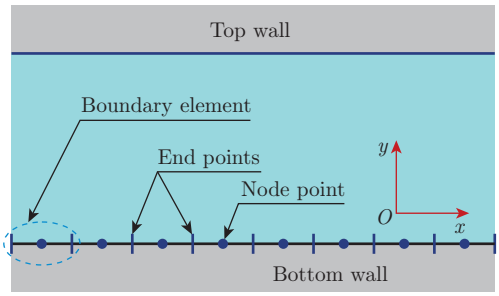

Fig. 6 Discretisation of the bottom wall by using boundary elements (color online)

Moreover, the aforementioned boundary values must also satisfy the boundary conditions (4) and (5). Referring to the work of Nieto et al.[25] and taking into account that $t_x(\boldsymbol{x}) = -n_y(\boldsymbol{x})$ and $t_y(\boldsymbol{x}) = n_x(\boldsymbol{x})$, the slip and no-penetration boundary conditions applied to all nodal points give rise to the following equations:

$$-u_i n_{yi} + v_i n_{xi} = \lambda_i(-\tau_i n_{yi} + \nu_i n_{xi} - \chi n_{xi}^2 + \chi n_{yi}^2), \tag{56}$$

$$u_i n_{xi} + v_i n_{yi} = 0, \tag{57}$$

where n_{xi} and n_{yi} are the two components of the outward unit vector $\boldsymbol{n}$ normal to the boundary at the ith node $\boldsymbol{x}_{0i}$ and the constant χ takes the value $\chi = H/2$ or $\chi = 1$ according as the flow is arbitrary or periodic.

By combining Eqs. (54)–(57), we obtain a system of linear equations as follows:

$$\boldsymbol{B}\boldsymbol{f} = \boldsymbol{q}, \tag{58}$$

where $\boldsymbol{f} = \{\tau_1, \tau_2, \cdots, \tau_{N^{\mathrm{B}}}, \nu_1, \nu_2, \cdots, \nu_{N^{\mathrm{B}}}, u_1, u_2, \cdots, u_{N^{\mathrm{B}}}, v_1, v_2, \cdots, v_{N^{\mathrm{B}}}\}^{\mathrm{T}}$ represents the vector of unknown boundary values, $\boldsymbol{B}$ is a matrix of size $4N^{\mathrm{B}} \times 4N^{\mathrm{B}}$, and $\boldsymbol{q}$ is a vector of size $1 \times 2N^{\mathrm{B}}$ whose values are provided in Appendix C[29].

The system of linear equations (58) is solved to obtain the values for τ_i, ν_i, u_i, and v_i at all nodal points. These values are then substituted into the following equation to determine the dimensionless effective slip length b:

$$b = \frac{\displaystyle\sum_{i=1}^{N^{\mathrm{B}}}(-u_i n_{yi} + v_i n_{xi})L_i}{\displaystyle\sum_{i=1}^{N^{\mathrm{B}}}(-\tau_i n_{yi} + \nu_i n_{xi} - \chi n_{xi}^2 + \chi n_{yi}^2)L_i}, \tag{59}$$

where $L_i = \displaystyle\int_{\Gamma_i} \mathrm{d}l_i$ is the length of the ith element. Notice that Einstein's summation convention does not apply in Eqs. (54)–(57) and (59).

5 Results and discussion

The methods elaborated in the previous sections are now used to study several examples of pressure-driven and shear-driven Stokes flows over a rough surface. In our computations, the normalized distance ϵ between the fictitious and physical boundaries is set to be equal to that between two neighboring collocation points. The fluid properties used in these numerical examples are provided in Table 1.

Table 1 Fluid properties and dimensions of the patch

Input	Value	Unit
Dynamic viscosity μ	10^{-3}	$\mathrm{Pa \cdot s}$
Mass density of fluid ϱ	10^3	$\mathrm{kg/m^3}$
x-component of pressure gradient ρ	10^3	$\mathrm{kN/m^3}$
Intrinsic slip length Λ	320	μm

5.1 Pressure-driven flow over a surface in the presence of a transverse groove

The first example consists of a 2D pressure-driven Stokes flow through a channel between two parallel walls. The top wall of the channel is smooth but the bottom wall is rough in the presence of a transverse groove. The normalized width of transverse grooves with respect to the length $\widehat{W}$ of the channel is set to be equal to 0.25. The interfacial zone occupied by the groove is assumed to be partially slippery and characterized by a normalized slip length $\lambda = 20$, while the rest of the bottom wall is assumed to be non-slippery with a zero slip length. Using the MFS, XMFS, and BEM, the variation of the normalized effective slip length in terms of the normalized channel thickness is first shown in Fig. 7 and then compared with the numerical ones obtained by the finite element method (FEM) using Comsol Multiphysics. Good agreement between these results can be observed, except the value at $H = 10$ and its neighbour obtained with the MFS. Particularly, unlike the MFS, XMFS, and FEM, it is seen in this figure that, by using the BEM, the effective slip length can be computed without difficulty when the channel is very thin, for example $H \leqslant 10^{-2}$.

5.2 Pressure-driven flow over a surface with periodically distributed transverse grooves

The second example concerns a pressure driven flow through a channel between two parallel walls, one of which is periodically rough and microtextured with transverse grooves. In this case, the slippery area fraction ϕ is taken to be equal to 0.75. As in the first example, the interfacial zone occupied by grooves is supposed to be partially slippery and characterized by a normalized slip length $\lambda = 20$. It is seen from Fig. 8 that very good agreement is achieved between the results obtained by applying the BEM and XMFM and the ones provided by Vinogradova and Balyaev[15]. The same remark can be made by comparing our results obtained with the numerical ones provided by the FEM.

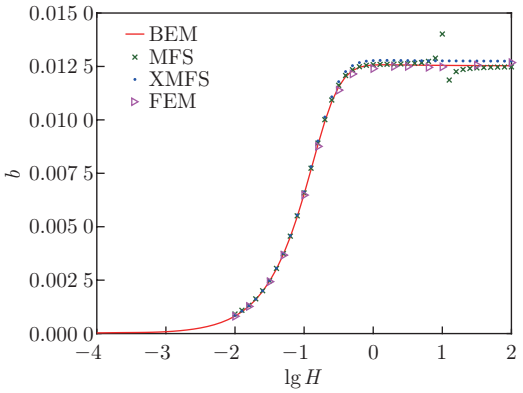

Fig. 7 Effective slip length versus the channel thickness for a pressure-driven flow over a transverse groove (color online)

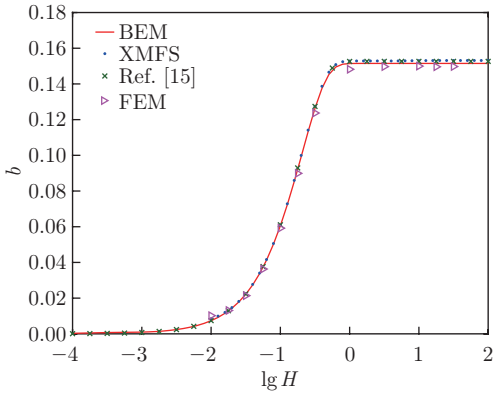

Fig. 8 Effective slip length versus the channel thickness for a pressure-driven flow over a surface with periodically distributed transverse grooves (color online)

5.3 Pressure-driven flow over a surface with randomly distributed transverse grooves

In this example, by applying the XMFS and BEM presented in the previous sections, the size of the RSE for a rough surface with randomly distributed transverse grooves can be determined. We consider a Stokes pressure-driven flow through a channel between two parallel walls, one of which is assumed to be rough with randomly distributed transverse grooves. More precisely, the interfacial zone occupied by grooves is supposed to be slippery with a normalized slip length

$\lambda = 20$, whereas the rest of the bottom interface is non-slippery. In the latter case, the slipping area fraction ϕ is kept constant and equal to $\phi = 0.5$, and the number of the grooves per unit length is taken to be equal to 50. At the macroscopic scale, the bottom rough interface is homogenized so as to be replaced by an equivalent smooth interface characterized by an effective slip length.

The average of the effective slip length corresponding to the rough surface with randomly distributed transverse grooves can be calculated by applying the Monte Carlo method, which was used in the works of Lachihab and Sab[30–31]. With K independent realizations of the microstructure of the rough surface, we denote by $(b_1, b_2, \cdots, b_K)$ the corresponding effective slip lengths. Then, the average of the effective slip length $\overline{b}$ is given by

$$\overline{b}_K = \frac{1}{K}(b_1 + b_2 + \cdots + b_K), \tag{60}$$

and the variance of the effective slip length is calculated by

$$\sigma_K^2 = \frac{1}{K-1}\sum_{i=1}^{K}(b_i - \overline{b}_K)^2. \tag{61}$$

The absolute and relative errors of the average value obtained are, respectively, defined by

$$\zeta_{\text{abs}} = 1.96\frac{\sigma_K}{\sqrt{K}}, \quad \zeta_{\text{rel}} = 1.96\frac{\sigma_K}{\overline{b}_K\sqrt{K}}. \tag{62}$$

With a sufficiently large value of K, the probability for the effective slip length $\overline{b}$ to be in the interval $[\overline{b}_K - \zeta_{\text{rel}}\overline{b}_K, \overline{b}_K + \zeta_{\text{rel}}\overline{b}_K]$ is 95%.

Figure 9 shows the influence of the size Π on the average of the effective slip lengths. These average values are plotted with their intervals of confidence $[\overline{b}_K - 1.96\sigma_K, \overline{b}_K + 1.96\sigma_k]$. Figure 10 indicates the number of realizations in terms of the size of the RSE. It is observed that the number of realizations decreases when the size of the RSE increases.

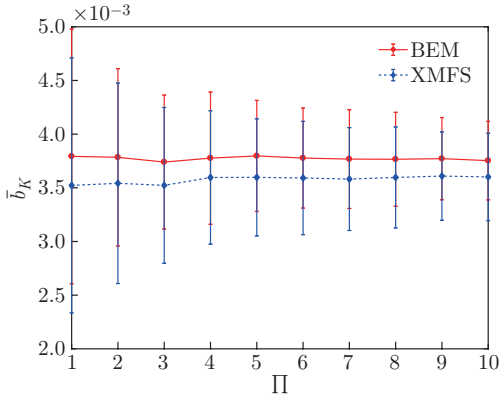

Fig. 9 Average value and confidence interval of the effective slip length versus the size of the RSE (color online)

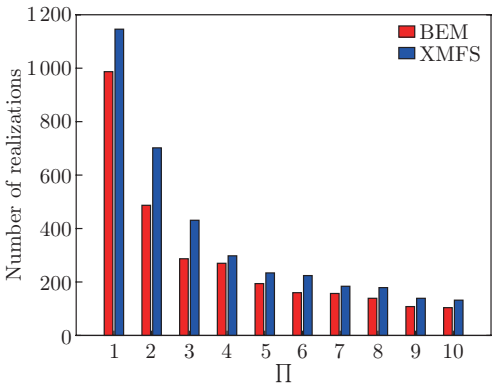

Fig. 10 Number of realizations versus the size of the RSE (color online)

5.4 Shear-driven flow over a surface with slip length varying according to a cosine function

In this example, we use both the XMFS and BEM to seek the solution of a 2D Couette flow over a periodically textured surface whose local normalized slip length takes the following dimensionless expression:

$$\lambda(x, 0) = \lambda_a + 2\lambda_b \cos(2\pi x), \tag{63}$$

where the two coefficients λ_a and λ_b are chosen to be such that $\lambda_a \geqslant 2\lambda_b \geqslant 0$.

We plot in Fig. 11 the values obtained for the normalized effective slip length b/λ_a by applying the BEM and XMFS in terms of the ratio λ_b/λ_a. Next, to validate the obtained results, these values are compared in Fig. 11 with those provided by Asmolov et al.[32]. Perfect agreement between these values can be observed in Fig. 11.

In Fig. 12, by varying the values of λ_a and λ_b in such a way that the ratio λ_b/λ_a is equal to 0.5, the normalized effective slip length $b/\widehat{W}$ is plotted versus the ratio $\lambda_a/\widehat{W}$. It can be seen from Fig. 12 that the results given by the XMFS and BEM coincide exactly with the analytical ones derived by Asmolov et al.[32].

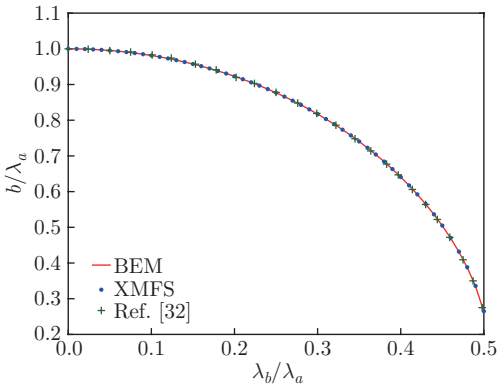

Fig. 11 Normalized effective slip length b/λ_a versus the ratio λ_b/λ_a of a flat surface whose local slip length is a cosinusoidal function $\lambda(x) = \lambda_a + 2\lambda_b \cos(2\pi x)$ (color online)

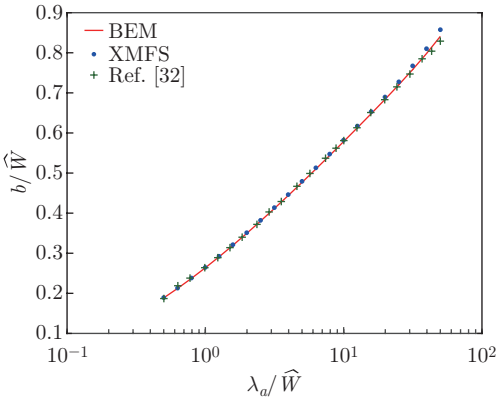

Fig. 12 Normalized effective slip length $b/\widehat{W}$ versus the ratio $\lambda_a/\widehat{W}$ of a flat surface whose local slip length is a cosinusoidal function $\lambda(x) = \lambda_a + 2\lambda_b \cos(2\pi x)$ with $\lambda_b/\lambda_a = 0.5$ (color online)

5.5 Shear-driven flow over a periodically corrugated surface

In the previous examples, the bottom surface was assumed to be rough at the micro- or nano-scale, since this is an origin of the liquid slippage phenomenon. At the mesoscopic and macroscopic levels, the interface between the wall and the fluid is taken to be flat and its roughness is accounted for by a slip boundary condition characterized by an intrinsic slip length. However, in many situations of practical importance, the solid surface may exhibit roughness at meso-scale and the influence of this roughness on the the flow properties cannot be neglected. This problem has been studied[33–39]. In the present example, the approach based on the BEM is now applied to study the problem mentioned above to test the efficiency and robustness of our approach. To this end, we consider a shear-driven flow over a periodically corrugated surface. At the meso-scale, the periodically corrugated surface is modeled as a sinusoidal wave but, at the macro-scale, this surface is considered to be flat. Our results will be compared with those presented by Niavarani and Priezjev[36].

In this study, the bottom wall has a sinusoidal corrugation described by

$$y(x) = a \sin(kx), \tag{64}$$

where $k = 2\pi$ denotes the wavenumber, and a is the corrugation amplitude. In Fig. 13, we show the variation of the effective slip length in terms of wavenumber ka obtained by using the BEM for the case where the local no-slip boundary condition is applied. These results are in good agreement with those of Ref. [36]. Particularly, the normalized velocity profiles shown in Fig. 14 for different values of ka such as $ka = 0$, 0.7, and 1.12 coincide perfectly with those derived by Niavarani and Priezjev[36].

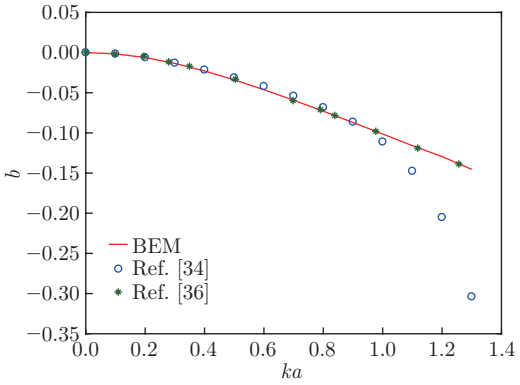

Fig. 13 Normalized effective slip length b versus the wavenumber ka of a non-slippery and sinusoidal surface $y(x) = a\sin(kx)$ (color online)

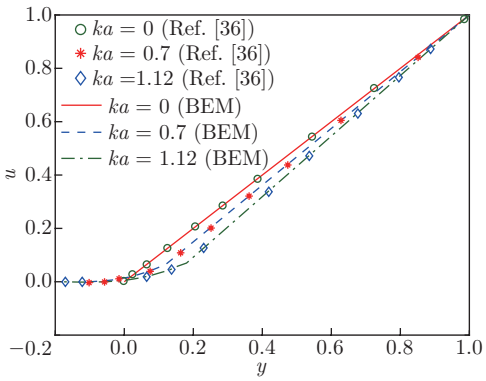

Fig. 14 Averaged velocity profiles of a shear-driven flow over a non-slippery and sinusoidal surface $y(x) = a\sin(kx)$ for three different wavenumber values $ka = 0$, $ka = 0.7$, and $ka = 1.12$ (color online)

The velocity profiles inside the valley obtained by the BEM and Niavarani and Priezjev[36] are displayed in Fig. 15. It can be seen from this figure that the velocity profiles inside the valley obtained by the BEM almost coincide with those provided in Ref. [36]. By setting the wavenumber to 1.12 and the local slip length at the corrugated wall to 0.03, Fig. 16 shows the velocity field and streamline of the shear-driven Stokes flow. We can observe in Fig. 16 that the vortex appears at the bottom of the valley. Next, in order to study the effect of the corrugated wall's surface on the velocity field and streamline of the Stokes flow, by varying the values of the local slip length such as $\lambda_0 = 0$, $\lambda_0 = 0.03$, $\lambda_0 = 0.06$, and $\lambda_0 = 0.08$, the corresponding streamlines in the valley are plotted in Fig. 17. It can be seen from Fig. 17 that the size of vortex inside the valley is reduced when the local slip length λ_0 is augmented. This phenomenon is completely in agreement with the observation about vortex provided in Ref. [36].

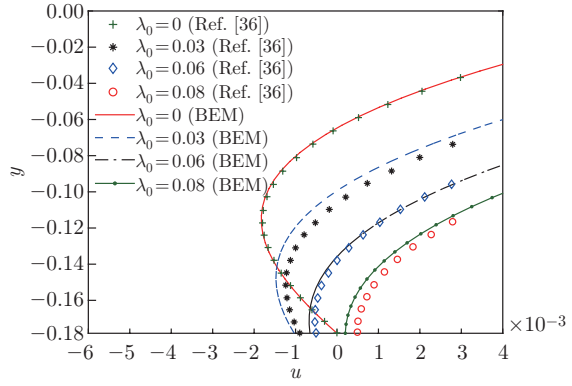

Fig. 15 Local velocity profiles inside the valley at $x = 0.75$ of a shear-driven flow over a sinusoidal surface $y(x) = a\sin(kx)$ for four different cases with $\lambda_0 = 0$, $\lambda_0 = 0.03$, $\lambda_0 = 0.06$, and $\lambda_0 = 0.08$ (color online)

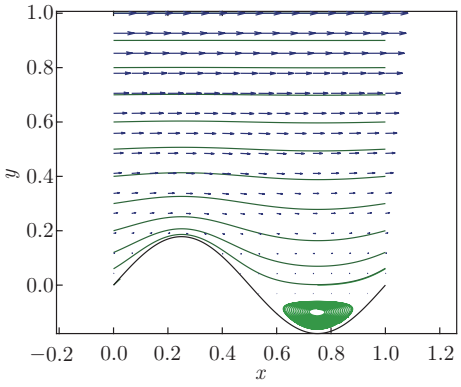

Fig. 16 Velocity field and streamline of a shear-driven fluid flow over a sinusoidal surface $y(x) = a\sin(kx)$ with the given wavenumber $ka = 1.12$ and the local slip length at the lower wall $\lambda_0 = 0.03$ (color online)

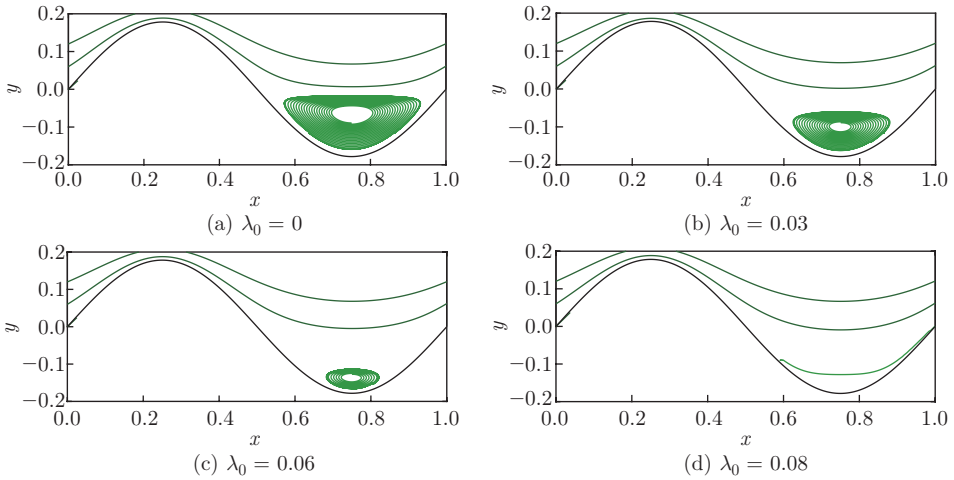

Fig. 17 Streamlines in the valley of a shear-driven fluid flow over a sinusoidal surface $y(x) = a\sin(kx)$ for four different values of the surfacial slip length $\lambda_0 = 0$, $\lambda_0 = 0.03$, $\lambda_0 = 0.06$, and $\lambda_0 = 0.08$ (color online)

We also plot in Figs. 18 and 19 the effective slip length b versus the local slip length λ_0 for two cases with

$$ka = 0.28, \quad \text{and} \quad ka = 1.12,$$

respectively. Our results are compared with those provided by Panzer et al.[34] and Niavarani and Priezjev[36]. More precisely, for the case where the wavenumber ka is equal to 1.12, good agreement between the values obtained by applying the BEM and Niavarani and Priezjev[36] is observed. For the case where the wavenumber ka equals 0.28, the results provided by the BEM is in perfect accord with those of Panzer et al.[34] and Niavarani and Priezjev[36] when $\lambda_0 \leqslant 1$. However, there is a small difference between them when the local slip length λ_0 increases.

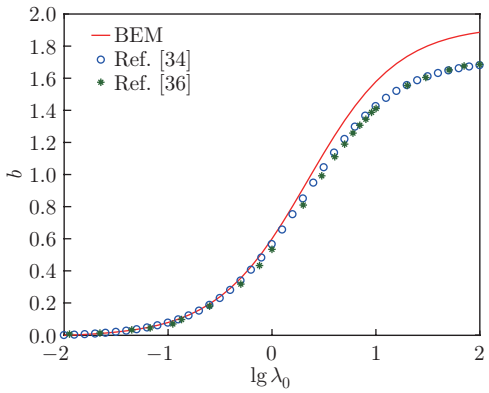

Fig. 18 Normalized effective slip length b versus the surfacial slip length $\lg\lambda_0$ of a sinusoidal surface $y(x) = a\sin(kx)$ with a given wavenumber $ka = 0.28$ (color online)

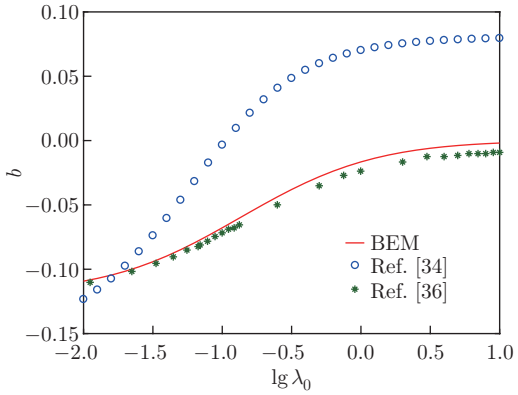

Fig. 19 Normalized effective slip length b versus the surfacial slip length $\lg\lambda_0$ of a sinusoidal surface $y(x) = a\sin(kx)$ with a given wavenumber $ka = 1.12$ (color online)

6 Conclusions

In this work, two numerical approaches based on the MFS or XMFS and BEM are elaborated to solve the problem of Stokes flow through a channel between two parallel walls of which one is rough and the other is smooth and non-slippery. In particular, the interface between the rough wall and fluid is homogenized so as to be replaced by an equivalent smooth slippery interface characterized by an effective slip length. The elaborated approaches hold in the general case where the distance between the two parallel walls can be arbitrary and the surface of one wall can be arbitrarily rough. This is in contrast with most of the available analytical and semi-analytical methods for the Stokes flow, which require that the channel thickness should be thin or/and the microstructure of the rough surface should be periodic.

The methods proposed in this paper can be extended to the case where the Stokes flow is produced through a 3D channel bounded by two parallel rough walls or a circular cylindrical rough wall. This work will be done in near future.

References

[1] TRAN, A. T., LE, Q. H., and HE, Q. C. Effective interfacial conditions for the Stokes flow of a fluid on periodically rough surfaces. *Acta Mechanica*, **228**, 1851–1869 (2017)

[2] LAUGA, K. and STONE, H. A. Effective slip in pressure-driven Stokes flow. *Journal of Fluid Mechanics*, **658**, 55–77 (2003)

[3] PRIEZJEV, N. V., DARHUBER, A. A., and TROIAN, S. M. Slip behavior on liquid films on surfaces of patterned wettability: comparison between continuum and molecular dynamics simulations. *Physical Review E*, **71**, 041608 (2005)

[4] NG, C. O. and WANG, C. Y. Stokes shear flow over a grating: implications for superhydrophobic slip. *Physics of Fluids*, **21**, 013602 (2009)

[5] NG, C. O. and WANG, C. Y. Apparent slip arising from Stokes shear flow over a bidimensional patterned surface. *Microfluidics and Nanofluidics*, **8**, 361–371 (2010)

[6] NG, C. O. and WANG, C. Y. Effective slip for Stokes flow over a surface patterned with two- or three-dimensional protrusions. *Fluid Dynamics Research*, **43**, 065504 (2011)

[7] KAMRIN, K., BAZANT, M. Z., and STONE, H. A. Effective slip boundary conditions for arbitrary periodic surfaces: the surface mobility tensor. *Journal of Fluid Mechanics*, **658**, 409–437 (2010)

[8] LUND, N. J., ZHANG, X. P., MAHELONA, K., and HENDY, S. C. Calculation of effective slip on rough chemically heterogeneous surfaces using a homogenization approach. *Physical Review E*, **86**, 046303 (2012)

[9] SBRAGAGLIA, M. and PROSPERETTI, A. A note on the effective slip properties for micro channel flows with ultra hydrophobic surfaces. *Physics of Fluids*, **19**, 043603 (2007)

[10] TEO, C. J. and KHOO, B. C. Analysis of Stokes flow in micro channels with superhydrophobic surfaces containing a periodic array of micro-grooves. *Microfluidics and Nanofluidics*, **7**, 353–382 (2009)

[11] CHENG, Y. P., TEO, C. J., and KHOO, B. C. Microchannel flows with superhydrophobic surfaces: effects of Reynolds number and pattern width to channel height ratio. *Physics of Fluids*, **21**, 122004 (2009)

[12] NG, C. O., CHU, H. C. W., and WANG, C. Y. On the effects of liquid-gas interfacial shear on slip flow through a parallel-plate channel with superhydrophobic grooved walls. *Physics of Fluids*, **22**, 102002 (2010)

[13] BELYAEV, A. V. and VINOGRADOVA, O. I. Effective slip in pressure-driven flow past superhydrophobic stripes. *Journal of Fluid Mechanics*, **652**, 489–499 (2010)

[14] NG, C. O. and CHU, H. C. W. Electrokinetic flows through a parallel-plate channel with slipping stripes on walls. *Physics of Fluids*, **23**, 102002 (2011)

[15] VINOGRADOVA, O. I. and BELYAEV, A. V. Wetting, roughness and flow boundary conditions. *Journal of Physics*: *Condensed Matter*, **23**, 184104 (2011)

[16] FEUILLEBOIS, F., BAZANT, M. Z., and VINOGRADOVA, O. I. Effective slip over superhydrophobic surfaces in thin channels. *Physical Review Letters*, **102**, 026001 (2009)

[17] ALVES, C. J. S. and SILVESTRE, A. L. Density results using Stokeslets and a method of fundamental solutions for the Stokes equations. *Engineering Analysis with Boundary Elements*, **28**, 1245–1252 (2004)

[18] YOUNG, D. L., JANE, S. J., FAN, C. M., MURUSEGAN, K., and TSAI, C. C. The method of fundamental solutions for 2D and 3D Stokes problems. *Journal of Computational Physics*, **211**, 1–8 (2006)

[19] ZHAO, S. and POVITSKY, A. Method of fundamental solutions for partial-slip fibrous filtration flows. *International Journal for Numerical Methods in Fluids*, **61**, 255–274 (2009)

[20] BOSELLI, F., OBRIST, D., and KLEISER, L. A mesh less boundary method for Stokes flows with particles: application to canalithiasis. *International Journal for Numerical Methods in Biomedical Engineering*, **29**, 1176–1191 (2013)

[21] ABOELKASSEM, Y. and STAPLES, A. E. Stokeslets-meshfree computations and theory for flow in a collapsible microchannel. *Theoretical and Computational Fluid Dynamics*, **27**, 681–700 (2013)

[22] POZRIKIDIS, C. Creeping flow in two-dimensional channels. *Journal of Fluid Mechanics*, **180**, 495–514 (1987)

[23] STABEN, M. E., ZINCHENKO, A. Z., and DAVIS, R. H. Motion of a particle between two parallel plane walls in low-Reynolds-number Poiseuille flow. *Physics of Fluids*, **15**, 1711–1733 (2003)

[24] JANSSEN, P. J. A. and ANDERSON, P. D. Boundary-integral method for drop deformation between parallel plates. *Physics of Fluids*, **19**, 043602 (2007)

[25] NIETO, C., GIRALDO, M., and POWER, H. Boundary integral method for Stokes flow with linear slip flow conditions in curved surfaces. *WIT Transactions on Modelling and Simulation*, **49**, 353–362 (2009)

[26] TLUPOVA, S. and CORTEZ, R. Boundary integral solutions of coupled Stokes and Darcy flows. *Journal of Computational Physics*, **228**, 158–179 (2009)

[27] POZRIKIDIS, C. *Boundary Integral and Singularity Methods for Linearized Viscous Flow*, Cambridge University Press, Cambridge (1992)

[28] GRIGGS, A. J., ZINCHENKO, A. Z., and DAVIS, R. H. Low-Reynolds-number motion of a deformable drop between two parallel plane walls. *International Journal of Multiphase Flow*, **33**, 182–206 (2007)

[29] KATSIKADELIS, J. T. *Boundary Elements*: *Theory and Applications*, Elsevier, Amsterdam (2002)

[30] LACHIHAB, A. and SAB, K. Aggregate composites: a contact based modeling. *Computational Materials Science*, **33**, 467–490 (2005)

[31] LACHIHAB, A. and SAB, K. Does a representative volume element exist for fatigue life prediction? The case of aggregate composites. *International Journal for Numerical and Analytical Methods in Geomechanics*, **32**, 1005–1021 (2008)

[32] ASMOLOV, E. S., SCHMIESCHEK, S., HARTING, J., and VINOGRADOVA, O. I. Flow past superhydrophobic surfaces with cosine variation in local slip length. *Physical Review E*, **87**, 023005 (2013)

[33] EINZEL, D., PANZER, P., and LIU, M. Boundary condition for fluid flow: curved or rough surfaces. *Physical Review Letters*, **64**, 2269–2272 (1990)

[34] PANZER, P., LIU, M., and EINZEL, D. The effects of boundary curvature on hydrodynamic fluid flow: calculation of slip lengths. *Physical Review Letters*, **64**, 2269–2272 (1992)

[35] NIAVARANI, A. and PRIEZJEV, N. V. Rheological study of polymer flow past rough surfaces with slip boundary conditions. *The Journal of Chemical Physics*, **129**, 144902 (2008)

[36] NIAVARANI, A. and PRIEZJEV, N. V. The effective slip length and vortex formation in laminar flow over a rough surface. *Physics of Fluids*, **21**, 052105 (2009)

[37] NIAVARANI, A. and PRIEZJEV, N. V. Modeling the combined effect of surface roughness and shear rate on slip flow of simple fluids. *Physical Review E*, **81**, 011606 (2010)

[38] PRIEZJEV, N. V. and TROIAN S. M. Influence of periodic wall roughness on the slip behaviour at liquid/solid interfaces: molecular-scale simulations versus continuum predictions. *Journal of Fluid Mechanics*, **554**, 25–46 (2006)

[39] GUO, L., CHEN, S., and ROBBINS, M. O. Effective slip boundary conditions for sinusoidally corrugated surfaces. *Physical Review Fluids*, **1**, 074102 (2016)

Appendix A Details for the matrix $\boldsymbol{A}$ and vector $\boldsymbol{c}$

The matrix $\boldsymbol{A}$ can be written as a combination of sub-matrices as follows:

$$\boldsymbol{A}=\begin{bmatrix}\boldsymbol{A}^{(1)} & \boldsymbol{A}^{(2)}\\ \boldsymbol{A}^{(3)} & \boldsymbol{A}^{(4)}\\ \boldsymbol{A}^{(5)} & \boldsymbol{A}^{(6)}\\ \boldsymbol{A}^{(7)} & \boldsymbol{A}^{(8)}\end{bmatrix}_{2N\times 2N}, \tag{A1}$$

where the components of the sub-matrices are given by

$$\begin{cases} A_{ij}^{(1)}=\dfrac{(x_i-\xi_j)^2}{r_{ij}^2}-\ln r_{ij}+\lambda_i\dfrac{(y_i-\eta_j)}{r_{ij}^2}+\lambda_i\dfrac{2(x_i-\xi_j)^2(y_i-\eta_j)}{r_{ij}^4},\\ A_{ij}^{(3)}=\dfrac{(x_i-\xi_j)(y_i-\eta_j)}{r_{ij}^2}, \end{cases} \tag{A2}$$

$$\begin{cases} A_{il}^{(2)}=\dfrac{(x_i-\xi_j)(y_i-\eta_j)}{r_{ij}^2}-\lambda_i\dfrac{(x_i-\xi_j)}{r_{ij}^2}+\lambda_i\dfrac{2(x_i-\xi_j)(y_i-\eta_j)^2}{r_{ij}^4},\\ A_{ij}^{(4)}=\dfrac{(y_i-\eta_j)^2}{r_{ij}^2}-\ln r_{ij} \end{cases} \tag{A3}$$

with $\boldsymbol{x}_i\ (x_i,y_i)\in\partial\Omega^{\mathrm{B}}$, $i=1,2,\cdots,N^{\mathrm{B}}$, and $j=1,2,\cdots,N$, and

$$\begin{cases} A_{ij}^{(5)}=\dfrac{(x_i-\xi_j)^2}{r_{ij}^2}-\ln r_{ij},\\ A_{ij}^{(6)}=A_{ij}^{(7)}=\dfrac{(x_i-\xi_j)(y_i-\eta_j)}{r_{ij}^2},\\ A_{ij}^{(8)}=\dfrac{(y_i-\eta_j)^2}{r_{ij}^2}-\ln r_{ij} \end{cases} \tag{A4}$$

with

$$\boldsymbol{x}_i(x_i,y_i)\in\partial\Omega^{\mathrm{T}},\quad i=1,2,\cdots,N^{\mathrm{T}},\quad j=1,2,\cdots,N.$$

The expression of the vector $\boldsymbol{c}$ is given by

$$\boldsymbol{c}=4\pi\chi\big[\underbrace{\lambda_1,\lambda_2,\cdots,\lambda_{N^{\mathrm{B}}}}_{1\times N^{\mathrm{B}}},\underbrace{0,\cdots,0}_{1\times N^{\mathrm{B}}},\underbrace{0,\cdots,0}_{1\times 2N^{\mathrm{T}}}\big]^{\mathrm{T}}, \tag{A5}$$

where $r_{ij}=\|\boldsymbol{x}_i-\boldsymbol{\xi}_j\|$ denotes the distance between the collocation point $\boldsymbol{x}_i$ and the source point $\boldsymbol{\xi}_j$.

Appendix B Details of the matrix $\boldsymbol{A}'$ and vector $\boldsymbol{c}'$

We can rewrite the matrix $\boldsymbol{A}'$ as follows:

$$\boldsymbol{A}'=\begin{bmatrix}\boldsymbol{A}'^{(1)} & \boldsymbol{A}'^{(2)}\\ \boldsymbol{A}'^{(3)} & \boldsymbol{A}'^{(4)}\end{bmatrix}_{2N^{\mathrm{B}}\times 2N^{\mathrm{B}}}, \tag{B1}$$

where the components of the sub-matrices are computed by

$$\begin{aligned}
A'^{(1)}_{ij} =& -\ln r_{ij} + \frac{(x_i-\xi_j)^2}{r_{ij}^2} + \ln R_{ij} - \frac{(x_i-\xi_j)^2}{R_{ij}^2} + \frac{2h_j^2}{R_{ij}^2} - \frac{4h_j^2(x_i-\xi_j)^2}{R_{ij}^4} \\
&- \frac{2h_j(y_i+\eta_j-2\omega)}{R_{ij}^2} + \frac{4h_j(x_i-\xi_j)^2(y_i+\eta_j-2\omega)}{R_{ij}^4} + \lambda_i\frac{2(x_i-\xi_j)^2(y_i-\eta_j)}{r_{ij}^4} \\
&+ \lambda_i\frac{(y_i-\eta_j)}{r_{ij}^2} - \lambda_i\frac{(y_i+\eta_j-2\omega)}{R_{ij}^2} - \lambda_i\frac{2(x_i-\xi_j)^2(y_i+\eta_j-2\omega)}{R_{ij}^4} \\
&+ \lambda_i\frac{4h_j^2(y_i+\eta_j-2\omega)}{R_{ij}^4} - \lambda_i\frac{16h_j^2(x_i-\xi_j)^2(y_i+\eta_j-2\omega)}{R_{ij}^6} - \lambda_i\frac{4h_j(x_i-\xi_j)^2}{R_{ij}^4} \\
&+ \lambda_i\frac{2h_j}{R_{ij}^2} - \lambda_i\frac{4h_j(y_i+\eta_j-2\omega)^2}{R_{ij}^4} + \lambda_i\frac{16h_j(x_i-\xi_j)^2(y_i+\eta_j-2\omega)^2}{R_{ij}^6}, \qquad \text{(B2)}
\end{aligned}$$

$$\begin{aligned}
A'^{(2)}_{ij} =& \frac{(x_i-\xi_j)(y_i-\eta_j)}{r_{ij}^2} - \frac{(x_i-\xi_j)(y_i+\eta_j-2\omega)}{R_{ij}^2} \\
&+ 4h_j^2\frac{(x_i-\xi_j)(y_i+\eta_j-2\omega)}{R_{ij}^4} - \frac{4h_j(x_i-\xi_j)(y_i+\eta_j-2\omega)^2}{R_{ij}^4} \\
&+ \lambda_i\frac{2(x_i-\xi_j)(y_i-\eta_j)^2}{r_{ij}^4} - \lambda_i\frac{2(x_i-\xi_j)(y_i+\eta_j-2\omega)^2}{R_{ij}^4} \\
&+ \lambda_i\frac{16h_j^2(x_i-\xi_j)(y_i+\eta_j-2\omega)^2}{R_{ij}^6} - \lambda_i\frac{4h_j^2(x_i-\xi_j)}{R_{ij}^4} + \lambda_i\frac{12h_j(x_i-\xi_j)(y_i+\eta_j-2\omega)}{R_{ij}^4} \\
&- \lambda_i\frac{16h_j(x_i-\xi_j)(y_i+\eta_j-2\omega)^3}{R_{ij}^6} - \lambda_i\frac{(x_i-\xi_j)}{r_{ij}^2} + \lambda_i\frac{(x_i-\xi_j)}{R_{ij}^2} + \frac{2h_j(x_i-\xi_j)}{R_{ij}^2}, \qquad \text{(B3)}
\end{aligned}$$

$$\begin{aligned}
A'^{(3)}_{ij} =& \frac{(x_i-\xi_j)(y_i-\eta_j)}{r_{ij}^2} - \frac{(x_i-\xi_j)(y_i+\eta_j-2\omega)}{R_{ij}^2} - \frac{4h_j^2(x_i-\xi_j)(y_i+\eta_j-2\omega)}{R_{ij}^4} \\
&+ \frac{2h_j(x_i-\xi_j)}{R_{ij}^2} + \frac{4h_j(x_i-\xi_j)(y_i+\eta_j-2\omega)^2}{R_{ij}^4}, \qquad \text{(B4)}
\end{aligned}$$

$$\begin{aligned}
A'^{(4)}_{ij} =& -\ln r_{ij} + \frac{(y_i-\eta_j)^2}{r_{ij}^2} + \ln R_{ij} - \frac{(y_i+\eta_j-2\omega)^2}{R_{ij}^2} + \frac{4h_j^2(y_i+\eta_j-2\omega)^2}{R_{ij}^4} \\
&+ \frac{2h_j(z+\nu_l-2\omega)}{R_{ij}^2} - \frac{4h_j(z+\nu_l-2\omega)^3}{R_{ij}^4} - \frac{2h_j^2}{R_{ij}^2}, \qquad \text{(B5)}
\end{aligned}$$

where

$$r_{ij} = \|\boldsymbol{x}_i - \boldsymbol{\xi}_j\|, \quad R_{ij} = \left\|\boldsymbol{x}_i - \boldsymbol{\xi}'_j\right\|, \quad i,j = 1,2,\cdots,N^{\mathrm{B}}.$$

The vector $\boldsymbol{c}'$ has the following expression:

$$\boldsymbol{c}' = 4\pi\chi\big[\underbrace{\lambda_1,\lambda_2,\cdots,\lambda_{N^{\mathrm{B}}}}_{1\times N^{\mathrm{B}}},\underbrace{0,\cdots,0}_{1\times N^{\mathrm{B}}}\big]^{\mathrm{T}}. \qquad \text{(B6)}$$

Appendix C Details of the matrix $\boldsymbol{B}$ and vector $\boldsymbol{q}$

The matrix $\boldsymbol{B}$ can in general be written in the following form:

$$\boldsymbol{B} = \begin{bmatrix} \boldsymbol{B}^{(1)} & \boldsymbol{B}^{(2)} & \boldsymbol{B}^{(3)} & \boldsymbol{B}^{(4)} \\ \boldsymbol{B}^{(5)} & \boldsymbol{B}^{(6)} & \boldsymbol{B}^{(7)} & \boldsymbol{B}^{(8)} \\ \boldsymbol{B}^{(9)} & \boldsymbol{B}^{(10)} & \boldsymbol{B}^{(11)} & \boldsymbol{B}^{(12)} \\ \boldsymbol{0} & \boldsymbol{0} & \boldsymbol{B}^{(13)} & \boldsymbol{B}^{(14)} \end{bmatrix}_{4N^{\mathrm{B}} \times 4N^{\mathrm{B}}}, \tag{C1}$$

where the sub-matrices of $\boldsymbol{B}$ are defined as follows:

$$B_{ij}^{(1)} = \frac{1}{4\pi} \int_{\Gamma_j} G_{xx}(\boldsymbol{x}_j, \boldsymbol{x}_{0i}) \mathrm{d}l_j, \quad B_{ij}^{(2)} = \frac{1}{4\pi} \int_{\Gamma_j} G_{yx}(\boldsymbol{x}_j, \boldsymbol{x}_{0i}) \mathrm{d}l_j, \tag{C2}$$

$$B_{ij}^{(3)} = \frac{1}{4\pi} \int_{\Gamma_j} (T_{xxx}(\boldsymbol{x}_j, \boldsymbol{x}_{0i}) n_x(\boldsymbol{x}_j) + T_{xxy}(\boldsymbol{x}_j, \boldsymbol{x}_{0i}) n_y(\boldsymbol{x}_j)) \mathrm{d}l_j + \frac{\delta_{ij}}{2}, \tag{C3}$$

$$B_{ij}^{(4)} = \frac{1}{4\pi} \int_{\Gamma_j} (T_{yxx}(\boldsymbol{x}_j, \boldsymbol{x}_{0i}) n_x(\boldsymbol{x}_j) + T_{yxy}(\boldsymbol{x}_j, \boldsymbol{x}_{0i}) n_y(\boldsymbol{x}_j)) \mathrm{d}l_j, \tag{C4}$$

$$B_{ij}^{(5)} = \frac{1}{4\pi} \int_{\Gamma_j} G_{xy}(\boldsymbol{x}_j, \boldsymbol{x}_{0i}) \mathrm{d}l_j, \quad B_{ij}^{(6)} = \frac{1}{4\pi} \int_{\Gamma_j} G_{yy}(\boldsymbol{x}_j, \boldsymbol{x}_{0i}) \mathrm{d}l_j, \tag{C5}$$

$$B_{ij}^{(7)} = \frac{1}{4\pi} \int_{\Gamma_j} (T_{xyx}(\boldsymbol{x}_j, \boldsymbol{x}_{0i}) n_x(\boldsymbol{x}_j) + T_{xyy}(\boldsymbol{x}_j, \boldsymbol{x}_{0i}) n_y(\boldsymbol{x}_j)) \mathrm{d}l_j, \tag{C6}$$

$$B_{ij}^{(8)} = \frac{1}{4\pi} \int_{\Gamma_j} (T_{yyx}(\boldsymbol{x}_j, \boldsymbol{x}_{0i}) n_x(\boldsymbol{x}_j) + T_{yyy}(\boldsymbol{x}_j, \boldsymbol{x}_{0i}) n_y(\boldsymbol{x}_j)) \mathrm{d}l_j + \frac{\delta_{ij}}{2}, \tag{C7}$$

$$B_{ij}^{(9)} = \lambda_i n_{yi} \delta_{ij}, \quad B_{ij}^{(10)} = -\lambda_i n_{xi} \delta_{ij}, \quad B_{ij}^{(11)} = -n_{yi} \delta_{ij}, \tag{C8}$$

$$B_{ij}^{(12)} = n_{xi} \delta_{ij}, \quad B_{ij}^{(13)} = n_{xi} \delta_{ij}, \quad B_{ij}^{(14)} = n_{yi} \delta_{ij}. \tag{C9}$$

The expressions of the matrix provided in Eqs. (C2)–(C7) require the evaluation of the line integral along the jth element. In this work, we distinguish the integral by considering the following two different cases:

(i) Off-diagonal elements, i.e., $i \neq j$

In this case, the evaluation points $\boldsymbol{x}_{0i}$ or $\boldsymbol{x}'_{0i}$ lie outside the jth element. This means that the distances r_{ij} and R_{ij} do not vanish, so that the above mentioned integrals are regular. For this reason, the standard Gaussian integration can be applied for their evaluation. This technique was described in detail in Ref. [29].

(ii) Diagonal elements, i.e., $i = j$

In this case, the evaluation points $\boldsymbol{x}'_{0i}$ still lie outside the jth element. Consequently, the standard Gaussian integration shall remain valid. However, the kernel functions of R_{ij} may be nearly singular when the channel height is very small. In addition, r_{ij} takes the value zero when the evaluation points $\boldsymbol{x}_{0i}$ and the integration point $\boldsymbol{x}_j$ coincide. Thus, the integrals involving r_{ij} can be singular. In the present work, the singular and near singular integrals have both been calculated analytically to overcome these drawbacks. In the analytical integration technique, for simplicity, all the special quantities should be taken into account, for example,

$$r_y = 0, \quad R_y = -2H, \quad h = -H, \quad n_x = 0, \quad n_y = -1. \tag{C10}$$

For arbitrary flow,

$$B_{ii}^{(1)} = \frac{L_i}{2}\ln\Big(\frac{16H^2+L_i^2}{L_i^2}\Big) - \frac{8H^2L_i}{16H^2+L^2} + 8H\arctan\Big(\frac{L_i}{4H}\Big), \tag{C11}$$

$$B_{ii}^{(2)} = B_{ii}^{(4)} = B_{ii}^{(5)} = B_{ii}^{(7)} = 0, \tag{C12}$$

$$B_{ii}^{(3)} = 4\arctan\Big(\frac{L_i}{4H}\Big) - \frac{16HL_i^3}{(16H^2+L_i^2)^2}, \tag{C13}$$

$$B_{ii}^{(6)} = \frac{L_i}{2}\ln\Big(\frac{16H^2+L_i^2}{L_i^2}\Big) - \frac{8H^2L_i}{16H^2+L^2}, \tag{C14}$$

$$B_{ii}^{(8)} = 4\arctan\Big(\frac{L_i}{4H}\Big) + \frac{16HL_i(32H^2+Li^2)}{(16H^2+L_i^2)^2}. \tag{C15}$$

For periodic flow,

$$\begin{aligned}
B_{ii}^{(1)} = {} & \frac{\mathrm{i}\pi^2}{3k} - \frac{\mathrm{i}kL_i^2}{8} - \frac{L_i}{2}\ln 4 + L_i\ln(1-\mathrm{e}^{\frac{\mathrm{i}kL_i}{2}}) - \frac{2\mathrm{iLi}_2\mathrm{e}^{\frac{\mathrm{i}kL_i}{2}}}{k} \\
& - \frac{L_i}{2}\ln\sin^2\frac{kL_i}{4} - \frac{1}{2}\mathrm{i}L_i\pi + \mathrm{i}H\ln(\mathrm{e}^{2Hk}-\mathrm{e}^{-\frac{\mathrm{i}kL_i}{2}}) \\
& - \frac{L_i}{4}\ln(\mathrm{e}^{2Hk}-\mathrm{e}^{-\frac{\mathrm{i}kL_i}{2}}) - \mathrm{i}H\ln(\mathrm{e}^{2Hk}-\mathrm{e}^{\frac{\mathrm{i}kL_i}{2}}) \\
& - \frac{\pi}{k}\ln(1+\mathrm{e}^{-\frac{\mathrm{i}kL_i}{2}}) - \frac{L_i}{4}\ln(\mathrm{e}^{2Hk}-\mathrm{e}^{\frac{\mathrm{i}kL_i}{2}}) \\
& + \frac{\pi}{k}\ln(1+\mathrm{e}^{\frac{\mathrm{i}kL_i}{2}}) - \mathrm{i}H\ln(1-\mathrm{e}^{2Hk-\frac{\mathrm{i}kL_i}{2}}) \\
& - \frac{L_i}{4}\ln(1-\mathrm{e}^{2Hk-\frac{\mathrm{i}kL_i}{2}}) + \mathrm{i}H\ln(1-\mathrm{e}^{2Hk+\frac{\mathrm{i}kL_i}{2}}) \\
& - \frac{L_i}{4}\ln(1-\mathrm{e}^{2Hk+\frac{\mathrm{i}kL_i}{2}}) + \frac{L_i}{2}\ln\Big(1+\mathrm{e}^{4Hk}-2\mathrm{e}^{2Hk}\cos\Big(\frac{kL_i}{2}\Big)\Big) \\
& + 4H\arctan\Big(\coth(Hk)\tan\Big(\frac{kL_i}{4}\Big)\Big) + \mathrm{i}H\ln\Big(-\mathrm{i}\sinh\Big(Hk-\frac{\mathrm{i}kL_i}{4}\Big)\Big) \\
& + \mathrm{i}H\ln\Big(\mathrm{i}\sinh\Big(Hk-\frac{\mathrm{i}kL_i}{4}\Big)\Big) - \mathrm{i}H\ln\Big(-\mathrm{i}\sinh\Big(Hk+\frac{\mathrm{i}kL_i}{4}\Big)\Big) \\
& - \mathrm{i}H\ln\Big(\mathrm{i}\sinh\Big(Hk+\frac{\mathrm{i}kL_i}{4}\Big)\Big) - \frac{\mathrm{iLi}_2(\mathrm{e}^{-2Hk-\frac{\mathrm{i}kL_i}{2}})}{2k} \\
& - \frac{\mathrm{iLi}_2(\mathrm{e}^{2Hk-\frac{\mathrm{i}kL_i}{2}})}{2k} + \frac{\mathrm{iLi}_2(\mathrm{e}^{-2Hk+\frac{\mathrm{i}kL_i}{2}})}{2k} + \frac{\mathrm{iLi}_2(\mathrm{e}^{2Hk+\frac{\mathrm{i}kL_i}{2}})}{2k} \\
& - H^2k\,\mathrm{csch}(Hk)\Big(\mathrm{csch}\Big(Hk-\frac{\mathrm{i}kL_i}{4}\Big) + \mathrm{csch}\Big(Hk+\frac{\mathrm{i}kL_i}{4}\Big)\Big)\sin\Big(\frac{kL_i}{4}\Big),
\end{aligned} \tag{C16}$$

$$B_{ii}^{(2)} = B_{ii}^{(4)} = B_{ii}^{(5)} = B_{ii}^{(7)} = 0, \tag{C17}$$

$$\begin{aligned}
B_{ii}^{(3)} = {} & 4H\arctan\Big(\coth(Hk)\tan\Big(\frac{kL_i}{4}\Big)\Big) + \frac{4H^2k^2\sin\Big(\frac{kL_i}{2}\Big)\sinh(2Hk)}{\Big(\cos\Big(\frac{kL_i}{2}\Big)-\cosh(2Hk)\Big)^2} \\
& - 2Hk\,\mathrm{csch}(Hk)\Big(\mathrm{csch}\Big(Hk-\frac{\mathrm{i}kL_i}{4}\Big) + \mathrm{csch}\Big(Hk+\frac{\mathrm{i}kL_i}{4}\Big)\Big)\sin\Big(\frac{kL_i}{4}\Big),
\end{aligned} \tag{C18}$$

$$
\begin{aligned}
B_{ii}^{(6)} \;=\; & \frac{\mathrm{i}\pi^2}{3k} - \frac{\mathrm{i}kL_i^2}{8} - \frac{L_i}{2}\ln 4 + L_i \ln\left(1-\mathrm{e}^{\frac{\mathrm{i}kL_i}{2}}\right) - \frac{2\mathrm{i}\mathrm{Li}_2(\mathrm{e}^{\frac{\mathrm{i}kL_i}{2}})}{k} - \frac{L_i}{4}\ln\left(\mathrm{e}^{2Hk}-\mathrm{e}^{-\frac{\mathrm{i}kL_i}{2}}\right) \\
& - \frac{L_i}{2}\ln\left(\sin^2\left(\frac{kL_i}{4}\right)\right) - \frac{1}{2}\mathrm{i}L_i\pi + \mathrm{i}H\ln\left(\mathrm{e}^{2Hk}-\mathrm{e}^{-\frac{\mathrm{i}kL_i}{2}}\right) - \mathrm{i}H\ln\left(\mathrm{e}^{2Hk}-\mathrm{e}^{\frac{\mathrm{i}kL_i}{2}}\right) \\
& - \frac{\pi}{k}\ln\left(1+\mathrm{e}^{-\frac{\mathrm{i}kL_i}{2}}\right) - \frac{L_i}{4}\ln\left(\mathrm{e}^{2Hk}-\mathrm{e}^{\frac{\mathrm{i}kL_i}{2}}\right) + \frac{\pi}{k}\ln\left(1+\mathrm{e}^{\frac{\mathrm{i}kL_i}{2}}\right) - \mathrm{i}H\ln\left(1-\mathrm{e}^{2Hk-\frac{\mathrm{i}kL_i}{2}}\right) \\
& + \mathrm{i}H\ln\left(1-\mathrm{e}^{2Hk+\frac{\mathrm{i}kL_i}{2}}\right) - \frac{L_i}{4}\ln\left(1-\mathrm{e}^{2Hk+\frac{\mathrm{i}kL_i}{2}}\right) - \frac{L_i}{4}\ln\left(1-\mathrm{e}^{2Hk-\frac{\mathrm{i}kL_i}{2}}\right) \\
& + \frac{L_i}{2}\ln\left(1+\mathrm{e}^{4Hk}-2\mathrm{e}^{2Hk}\cos\left(\frac{kL_i}{2}\right)\right) - 4H\arctan\left(\coth(Hk)\tan\left(\frac{kL_i}{4}\right)\right) \\
& + \mathrm{i}H\ln\left(-\mathrm{i}\sinh\left(Hk-\frac{\mathrm{i}kL_i}{4}\right)\right) + \mathrm{i}H\ln\left(\mathrm{i}\sinh\left(Hk-\frac{\mathrm{i}kL_i}{4}\right)\right) \\
& - \mathrm{i}H\ln\left(-\mathrm{i}\sinh\left(Hk+\frac{\mathrm{i}kL_i}{4}\right)\right) - \mathrm{i}H\ln\left(\mathrm{i}\sinh\left(Hk+\frac{\mathrm{i}kL_i}{4}\right)\right) \\
& - \frac{\mathrm{i}\mathrm{Li}_2(\mathrm{e}^{-2Hk-\frac{\mathrm{i}kL_i}{2}})}{2k} - \frac{\mathrm{i}\mathrm{Li}_2(\mathrm{e}^{2Hk-\frac{\mathrm{i}kL_i}{2}})}{2k} + \frac{\mathrm{i}\mathrm{Li}_2(\mathrm{e}^{-2Hk+\frac{\mathrm{i}kL_i}{2}})}{2k} + \frac{\mathrm{i}\mathrm{Li}_2(\mathrm{e}^{2Hk+\frac{\mathrm{i}kL_i}{2}})}{2k} \\
& - H^2 k\,\mathrm{csch}(Hk)\Big(\mathrm{csch}\Big(Hk-\frac{\mathrm{i}kL_i}{4}\Big) + \mathrm{csch}\Big(Hk+\frac{\mathrm{i}kL_i}{4}\Big)\Big)\sin\Big(\frac{kL_i}{4}\Big), \qquad \text{(C19)}
\end{aligned}
$$

$$
\begin{aligned}
B_{ii}^{(8)} \;=\; & 4H\arctan\left(\coth(Hk)\tan\left(\frac{kL_i}{4}\right)\right) + \frac{4H^2k^2\sin\left(\frac{kL_i}{2}\right)\sinh(2Hk)}{\left(\cos\left(\frac{kL_i}{2}\right)-\cosh(2Hk)\right)^2} \\
& + 2Hk\,\mathrm{csch}(Hk)\Big(\mathrm{csch}\Big(Hk-\frac{\mathrm{i}kL_i}{4}\Big) + \mathrm{csch}\Big(Hk+\frac{\mathrm{i}kL_i}{4}\Big)\Big)\sin\Big(\frac{kL_i}{4}\Big), \qquad \text{(C20)}
\end{aligned}
$$

where L_i denotes the length of ith element, $\mathrm{i}=\sqrt{-1}$, and $\mathrm{Li}_2(z)$ stands for the poly-logarithm function of order 2 and argument z.

The vector $\boldsymbol{q}$ is defined by

$$
\boldsymbol{q} = (\underbrace{0,\cdots,0}_{1\times 2N^{\mathrm{B}}}, \underbrace{\lambda_1\chi(n_{y1}^2-n_{x1}^2),\cdots,\lambda_{N^{\mathrm{B}}}\chi(n_{yN^{\mathrm{B}}}^2-n_{xN^{\mathrm{B}}}^2)}_{1\times N^{\mathrm{B}}}, \underbrace{0,\cdots,0}_{1\times N^{\mathrm{B}}})^{\mathrm{T}}. \qquad \text{(C21)}
$$